remote sensing

MDPI

Article

A Spatio-Temporal Fusion Method for Mine Subsidence Based on Decoupling the Basic Deformation Field from Residuals Using InSAR-GNSS

Xu Yang [1,2,3,4,5,*], Zhenyuan He [1,2,3,4,5], Jiajia Yuan [1,2,3,4,5], Mingfei Zhu [1,2,3,4,5], Xuexiang Yu [1,2,3,4,5], Lei Wang [1,2,3,4,5], Yulong Ge [6] and Shuai Nie [7]

1 Key Laboratory of Aviation-Aerospace-Ground Cooperative Monitoring and Early Warning of Coal Mining-Induced Disasters of Anhui Higher Education Institutes, Anhui University of Science and Technology, KLAHEI (KLAHEI18015), Huainan 232001, China; zhenyuan.he@aust.edu.cn (Z.H.); yuanjiajia@aust.edu.cn (J.Y.); zhumingfei@aust.edu.cn (M.Z.); xxyu@aust.edu.cn (X.Y.); lwang@aust.edu.cn (L.W.)
2 State Key Laboratory for Safe Mining of Deep Coal Resources and Environment Protection, Anhui University of Science and Technology, Huainan 232001, China
3 Engineering Research Center of Mining Area Environmental and Disaster Cooperative Monitoring, Anhui University of Science and Technology, Huainan 232001, China
4 School of Geomatics, Anhui University of Science and Technology, Huainan 232001, China
5 Urban 3D Real Scene and Intelligent Security Monitoring Joint Laboratory of Anhui Province, Huainan 232001, China
6 School of Marine Science and Engineering, Nanjing Normal University, Nanjing 210023, China; geyulong@njnu.edu.cn
7 School of Systems Science and Engineering, Sun Yat-Sen University, Guangzhou 510275, China; niesh5@mail2.sysu.edu.cn
* Correspondence: xyang@aust.edu.cn

Highlights

What are the main findings?

- BR-STKF achieves root mean square errors of 6.37 mm (strict spatial LOOCV) and 2.84 mm (retrospective with missing InSAR), demonstrating competitive and robust performance compared with existing benchmark models.
- Baseline–residual decoupling with GNSS correlation anchoring and Helmert variance component estimation improves daily scale LOS reconstruction.

What are the implications of the main findings?

- The framework effectively combines InSAR spatial coverage with daily GNSS observations for mining subsidence monitoring.
- It offers a feasible spatio-temporal fusion strategy for large-gradient, nonlinear deformation, though further independent validation is needed.

Academic Editor: Antonio Miguel Ruiz Armenteros

Received: 21 September 2026
Revised: 30 October 2026
Accepted: 3 November 2026
Published: 4 November 2026

Copyright: © 2026 by the authors. Licensee MDPI, Basel, Switzerland. This article is an open access article distributed under the terms and conditions of the Creative Commons Attribution (CC BY) license.

Abstract

Ground surface subsidence resulting from underground mining is characterized by significant spatial deformation gradients and nonlinear temporal deformation. A single monitoring technique is insufficient to simultaneously achieve extensive spatial coverage and high temporal continuity. Interferometric Synthetic Aperture Radar (InSAR) provides high spatial resolution but is limited by sparse temporal sampling, whereas the Global Navigation Satellite System (GNSS) offers dense temporal sampling but with restricted spatial coverage. To address these limitations, this study introduces a spatio-temporal fusion method combining InSAR and GNSS, based on baseline deformation

field–residual decoupling (BR-STKF), specifically applied to the Banji Coal Mine in the Huainan Mining Area, Anhui Province. Sentinel-1 SBAS-InSAR is employed to derive Line-Of-Sight (LOS) deformation time series, while three-dimensional GNSS displacements are projected onto the LOS direction. A daily scale baseline deformation field is constructed using pixel-wise Kalman filtering and Rauch–Tung–Striebel (RTS) smoothing. Subsequently, residual signals between the InSAR/GNSS observations and the baseline field are estimated utilizing a correlation-anchored multiscale spatial basis and an information-form Kalman filter. Helmert variance component estimation is introduced to adaptively adjust the weights of InSAR and GNSS observations. To demonstrate the reliability of the proposed framework, a quantitative validation was conducted. The experimental results yielded root mean square error (RMSE) values of 6.37 mm for strict spatial leave-one-out cross-validation (LOOCV) and 2.84 mm for retrospective reconstruction with missing InSAR phases. These results are competitive and comparable to leading benchmarks such as the Spatio-Temporal Kalman Filter (STKF), while achieving lower mean RMSEs than baseline methods such as Spatio-Temporal Random Effects (STREs), Enhanced Spatio-Temporal Random Effects (eSTREs), Improved Spatio-Temporal Random Effects (ISTREs), Multi-resolution Orthogonal Polynomial Basis (MOP), and ST-Kriging. However, the statistical stability of differences among models requires further verification with additional independent data. The findings suggest that the baseline deformation field–residual decoupling strategy effectively integrates the spatial coverage of InSAR with daily GNSS observations, offering a viable framework for daily scale line-of-sight (LOS) deformation reconstruction in mining areas.

Keywords: mine subsidence monitoring; InSAR; GNSS; spatio-temporal fusion; multi-scale spatial basis

1. Introduction

Underground mining in mining areas can easily trigger the movement of overlying strata in goaf zones and cause ground subsidence, leading to problems such as ground collapse, water accumulation, building deformation, and ecological damage. Continuous and detailed monitoring of subsidence in mining areas is a crucial foundation for safe mining operations, disaster risk prevention and control, and ecological restoration in mining areas [1–5].

Geodetic techniques such as traditional leveling, total stations, and the Global Navigation Satellite System (GNSS) offer high single-point accuracy but involve substantial fieldwork and have limited spatial coverage, making it difficult to meet the requirements for continuous monitoring of large-scale subsidence fields [6,7]. Interferometric Synthetic Aperture Radar (InSAR) technology offers the capability for large-area, areal, and high-spatial-resolution observations and has been widely applied to surface deformation monitoring in mining areas and urban environments [8–16]. However, InSAR primarily captures deformation along the radar Line Of Sight (LOS) and is affected by factors such as satellite revisit periods, spatio-temporal decoherence, atmospheric delay, and phase unwrapping errors. Consequently, issues such as insufficient temporal continuity and localized data gaps still exist in high-gradient mining area subsidence fields.

Therefore, integrating the complementary advantages of InSAR and GNSS to construct deformation time series that combine high spatial resolution with high temporal continuity represents an important research direction for mining area subsidence monitoring.

Existing research on InSAR-GNSS fusion primarily focuses on the following cate-

gories: first, using GNSS to correct InSAR atmospheric or ionospheric delays to improve the accuracy of InSAR time-series deformation [17–21]; second, using multi-track InSAR, GNSS, and spatial interpolation methods to invert 3D deformation or improve spatial resolution [22,23]; third, conducting subsidence inversion by combining physical models of mining operations, such as probabilistic integration models [24–27]; and fourth, using spatio-temporal random effect models, Kalman filters (KF), or adaptive spatial basis functions to achieve high spatio-temporal resolution deformation reconstruction [28–33].

Although significant progress has been made with the above methods, three challenges remain in mining areas—scenarios characterized by strong nonlinear deformation, large spatial gradients, and complex observation noise. First, the sparse InSAR time series and daily GNSS observations tend to create an imbalance in observation information during joint filtering; second, sparse GNSS stations struggle to reliably constrain large-scale spatial extrapolation; and third, empirically determined InSAR/GNSS observation weights fail to accurately reflect the actual noise levels of specific datasets.

For instance, conventional methods relying on isotropic spatial bases or fixed smoothing parameters (e.g., standard STRE or ST-Kriging) tend to over-smooth steep subsidence rims, thereby truncating sharp spatial gradients. Furthermore, during rapid non-linear accelerations with InSAR temporal gaps, traditional linear interpolation or static filters introduce artificial velocity discontinuities and fail to adapt to dynamic noise variations.

To address the above issues, this paper proposes an InSAR-GNSS spatio-temporal fusion framework that combines pixel-by-pixel Kalman smoothing, multiscale spatial basis functions, and Helmert variance component estimation [34–36]. This framework decomposes the fusion process into two stages: "baseline deformation field construction" and "residual field estimation." In the first stage, a daily scale baseline deformation field is constructed from sparse InSAR time series. In the second stage, InSAR and GNSS residual signals are jointly estimated within a correlation-anchored multiscale spatial basis.

The main contributions of this paper include: (1) proposing a fusion strategy that decouples the baseline deformation field from the residuals to mitigate information imbalance caused by differences in spatio-temporal sampling between InSAR and GNSS; (2) constructing a correlation-anchored multiscale Bi-square spatial basis to enhance local constraints under sparse GNSS conditions; and (3) introducing Helmert variance component estimation to adjust the relative weights of the two types of observations based on predicted residuals, and evaluating model performance through full fitting, station-retained reconstruction with a fixed spatial basis structure, and retrospective reconstruction of missing InSAR phases.

To address the aforementioned methodological bottlenecks, this paper proposes a general and independent InSAR-GNSS spatio-temporal fusion framework based on baseline–residual decoupling (BR-STKF). While the Banji Coal Mine in the Huainan Mining Area is adopted as a rigorous application testbed to evaluate its performance under large-gradient mining deformation, the proposed BR-STKF framework is mathematically structured as a decoupled, modular system that can be generalized to other geodetic fusion scenarios.

2. Materials and Methods

2.1. Overview of the Study Area

The study area in this paper is located at the Banji Coal Mine in Lixin County, Bozhou City, Anhui Province, China, and is one of the major mines in the Huainan Mining Area, as shown in Figure 1.

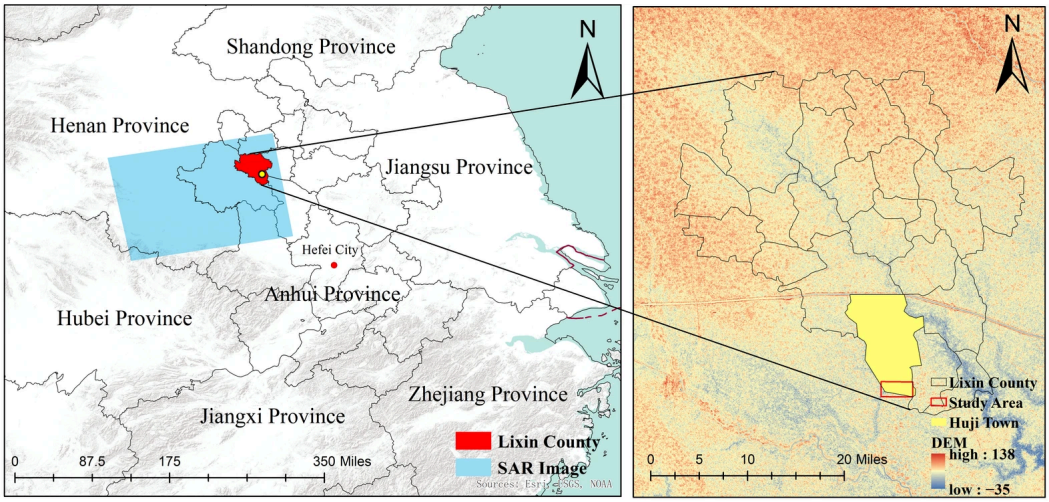


Figure 1. Geographic location of the study area and multiscale regional context.

The geographic extent of the study area is approximately 116°11′00″E–116°24′00″E and 32°50′30″N–32°57′20″N. The mine covers an area of approximately 32 km^2, with coal reserves of about 506 million metric tons and a designed annual production capacity of approximately 3 million metric tons. A detailed overview of the study area is shown in Figure 2.



Figure 2. Google Maps imagery of the Banji Coal Mine study area and an overview of the GNSS stations used. The red box indicates the boundary of the study area.

Furthermore, the Banji Coal Mine is characterized by a very thick layer of loose overburden and deep-well mining [37]. Under such geological and mining conditions, consolidation compression, drainage and recharge of the bottom aquifer, and mining-induced disturbances may interact to cause the mine area's subsidence to exhibit a phased temporal evolution.

2.2. Data and Preprocessing

This study utilized publicly released Single Look Complex (SLC) data from the European Space Agency's (ESA) Sentinel-1 A in the Interferometric Wide Swath (IW) mode, covering the period from 15 August 2022 to 3 September 2023, comprising a total

of 32 scenes with a revisit period of approximately 12 days. Supplementary data included Precision Orbit Data (POD) and the Copernicus DEM GLO-30. GNSS data were derived from daily coordinate solutions provided by continuous GNSS monitoring stations within the study area as part of the automated monitoring system. A total of 11 GNSS monitoring stations were established within the study area; however, the monitoring periods for some stations were too short to align with the SAR timeframe used in this study. Therefore, three-dimensional coordinate data from five GNSS monitoring stations—whose monitoring periods matched the SAR timeframe—were selected for the data fusion analysis.

GNSS monitoring stations provide daily 3D coordinates for each site. To ensure consistency with InSAR LOS-oriented deformation, the east, north, and zenith displacements from the GNSS data must be unified into a single reference frame and projected onto the LOS direction based on Sentinel-1's angle of incidence and heading angle.

Given that the study area is affected by underground coal mining, this study employs the Small Baseline Subset Interferometric Synthetic Aperture Radar (SBAS-InSAR) method for time-series deformation inversion. SBAS-InSAR mitigates the effects of incoherence by constructing a short spatio-temporal baseline interferometric network and addresses rank deficiency issues in the interferometric network using strategies such as singular value decomposition; it has been widely used for surface subsidence monitoring in mining areas [38–40].

In the specific processing, this paper performs time-series analysis on Sentinel-1 interferometric sequences using MintPy [41]. The processing workflow includes steps such as orbit error correction, topographic phase removal, phase unwrapping, time-series inversion, and geocoding, combined with spatio-temporal filtering to suppress residual atmospheric delay and high-frequency noise. To construct the observation network required for SBAS-InSAR time-series inversion, this paper screens interferogram pairs based on spatial and temporal baseline thresholds, forming a spatio-temporal baseline network and an interferogram network, as shown in Figure 3. This network provides the interferogram network connectivity required for subsequent phase disentanglement and time-series inversion. Specifically, the temporal baseline threshold was set to 60 days and the spatial baseline threshold to 200 m, resulting in a total of 124 interferometric pairs.

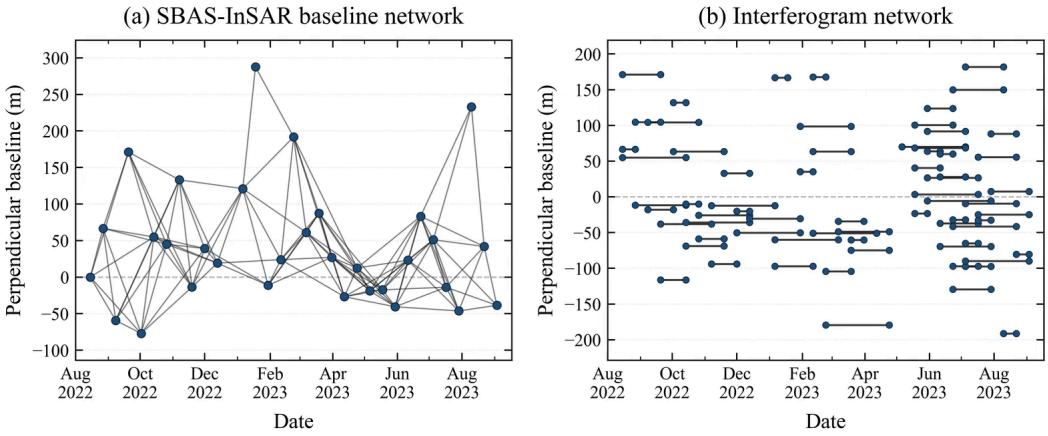


Figure 3. SBAS-InSAR baseline network and interferogram network: (**a**) spatio-temporal baseline network; (**b**) interferogram network.

The basic processing workflow for SBAS-InSAR is as follows:

For N SAR images from the same region at different time phases, the time series is t_1, t_2,…, t_N. An image from the reference time phase t_0 is selected as the reference image. The other images are then interferometrically processed with the reference image. At the

same time, thresholds for spatial and temporal baselines are set to select M interferometric pairs. The number of images N and the number of interferometric pairs M satisfy:

$$\frac{N}{2} \leq M \leq \frac{N(N-1)}{2} \tag{1}$$

The observed phase information for each corresponding interference pair is:

$$\Delta\phi_k(x,y) = \phi_k^{obs}(x,y) \ \ mod 2\pi \tag{2}$$

where $k = 1, 2, \ldots, M$, (x, y) are pixel coordinates, and $\Delta\varphi_k^{obs}$ is the unwrapped phase, typically solved using the minimum cost flow or branch-and-cut algorithms.

The phase sequence matrix is an $M \times P$ matrix (where P is the number of pixels):

$$\Delta\phi^{obs} = [\Delta\phi_1, \Delta\phi_2, \ldots, \Delta\phi_M]^T \tag{3}$$

Based on the above interferometric phase model, SBAS-InSAR screens for high-quality interferometric pairs and corrects the phase contribution terms to ultimately invert and obtain the LOS-direction cumulative deformation time series for the study area. The specific processing workflow for interferometric and temporal InSAR is shown in Figure 4.

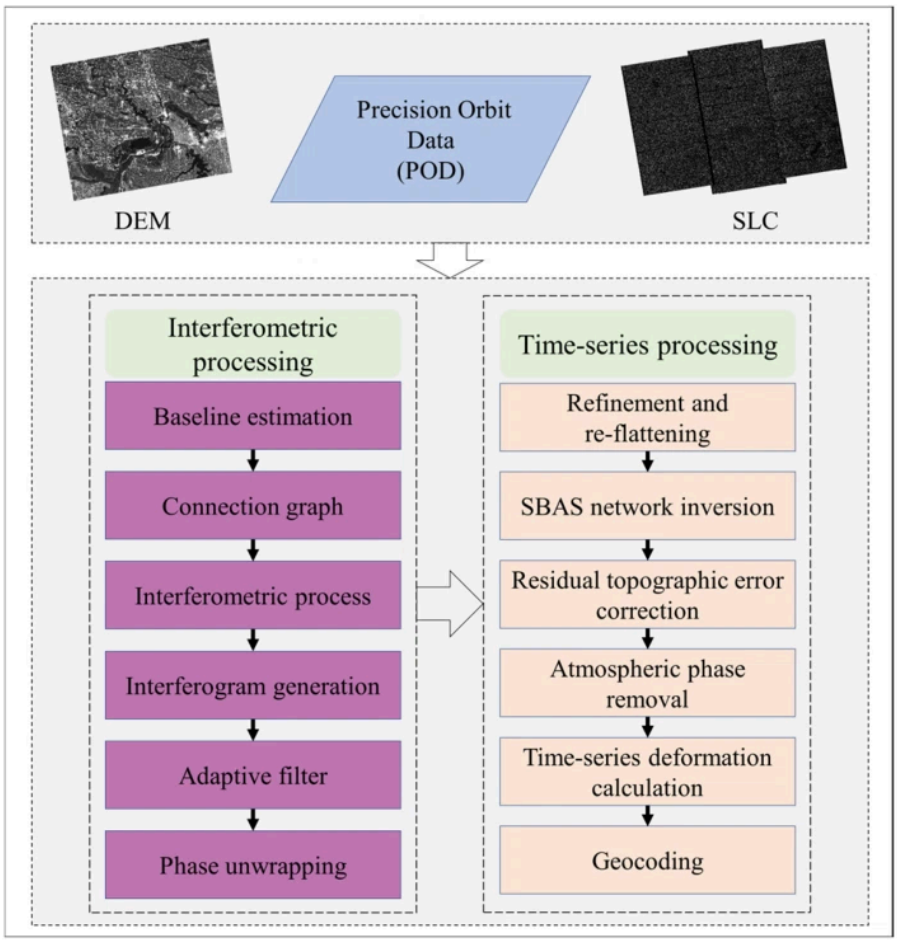


Figure 4. SBAS-InSAR data processing workflow.

The composition of the InSAR phase can be divided into five main parts:

$$\psi = \varphi_{topo} + \varphi_{def} + \varphi_{atm} + \varphi_{orbit} + \varphi_{noi} \quad (4)$$

Among these, φ_{topo} represents the terrain phase, φ_{def} represents the deformation phase, φ_{atm} represents the atmospheric phase, φ_{orbit} represents the orbital phase, and φ_{noi} represents the noise phase.

Among these, the deformation phase primarily reflects the cumulative displacement along the line of sight (LOS); the terrain phase is mainly caused by DEM errors; the orbit phase typically manifests as a spatially low-frequency, temporally slow-varying component; the atmospheric phase exhibits spatially high-frequency, temporally slow-varying characteristics; and the noise phase primarily originates from thermal noise and image registration errors.

Commonly used InSAR time-series processing platforms include the commercial software SARscape and open-source software such as MintPy and StaMPS. This paper selected MintPy for SBAS-InSAR processing because its workflow is transparent, its parameters are traceable, and it facilitates integration with subsequent InSAR-GNSS fusion models.

This study utilizes high-precision orbit files to correct orbital phase errors, employs the Copernicus DEM GLO-30 to remove the influence of topographic phase, and uses MintPy's time-series inversion and spatio-temporal filtering modules to estimate linear deformation rates, DEM errors, and residual atmospheric delays.

Since this paper uses only single-track Sentinel-1 data, the InSAR observations primarily reflect deformation in the line-of-sight (LOS) direction, whereas GNSS provides three-dimensional displacement information. Therefore, before data fusion, it is necessary to unify the spatial reference frame and project the GNSS three-dimensional displacements onto the InSAR LOS direction. The relevant transformation relationships are shown in Figure 5.

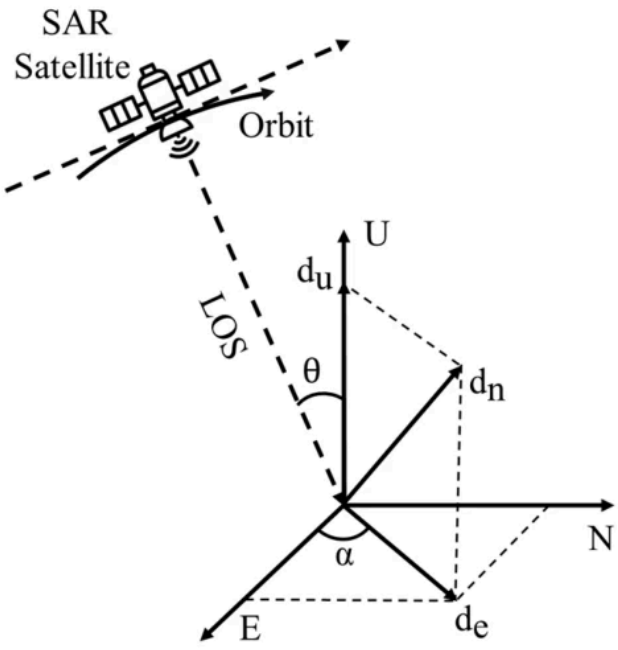


Figure 5. Schematic diagram of the geometric relationship between the GNSS 3D displacement and its LOS-direction projection.

The transformation relationship between GNSS 3D displacement and LOS-direction displacement is as follows [42]:

$$d_{los} = d_u cos\theta - d_e sin\theta \cdot sin\left(\alpha - \frac{3\pi}{2}\right) - d_n sin\theta \cdot cos\left(\alpha - \frac{3\pi}{2}\right) \quad (5)$$

where θ is the satellite orbital incidence angle, α is the satellite orbital heading angle, d_{los} is the LOS displacement resulting from the projection of the GNSS 3D displacement, and d_u, d_e, and d_n are the vertical, eastward, and northward displacement components, respectively.

To test the fusion capability of InSAR and GNSS data, this paper matches adjacent InSAR pixels with GNSS station coordinates and calculates the Pearson correlation coefficient (PCC) and root mean square error (RMSE) for valid epochs in the same time period.

The calculation of the PCC is as follows:

$$r = \frac{\sum_{i=1}^{n}\left(G_i - \overline{G}\right)\left(I_i - \overline{I}\right)}{\sqrt{\sum_{i=1}^{n}\left(G_i - \overline{G}\right)^2} \cdot \sqrt{\sum_{i=1}^{n}\left(I_i - \overline{I}\right)^2}} \quad (6)$$

where G_i and I_i are the GNSS LOS value and the InSAR LOS value corresponding to the i-th common epoch, respectively; $\overline{G}$ and $\overline{I}$ are the averages of the GNSS LOS values and the InSAR LOS values corresponding to all epochs; n is the number of epochs valid for both; and r is the Pearson correlation coefficient, with a range of [−1, 1].

Calculation of the RMSE between InSAR and GNSS:

$$RMSE = \sqrt{\frac{1}{n}\sum_{i=1}^{n}\left(G_i I_i\right)^2} \quad (7)$$

The RMSE is calculated based only on observation epochs where both GNSS and InSAR data are valid.

Figure 6 shows a comparison of LOS deformation time series between GNSS and adjacent InSAR pixels. It can be seen that the five GNSS stations and adjacent InSAR pixels generally exhibit consistent trends in LOS changes; the RMSE for the corresponding time periods ranges from 2.48 to 8.50 mm. Differences in inter-station correlation and local variations still exist, indicating that fusion requires the introduction of correlation anchoring and weight calibration, rather than relying solely on nearest-neighbor pixels. Therefore, this study employs a multiscale spatial basis with correlation anchoring to construct the basic deformation field of the study area.

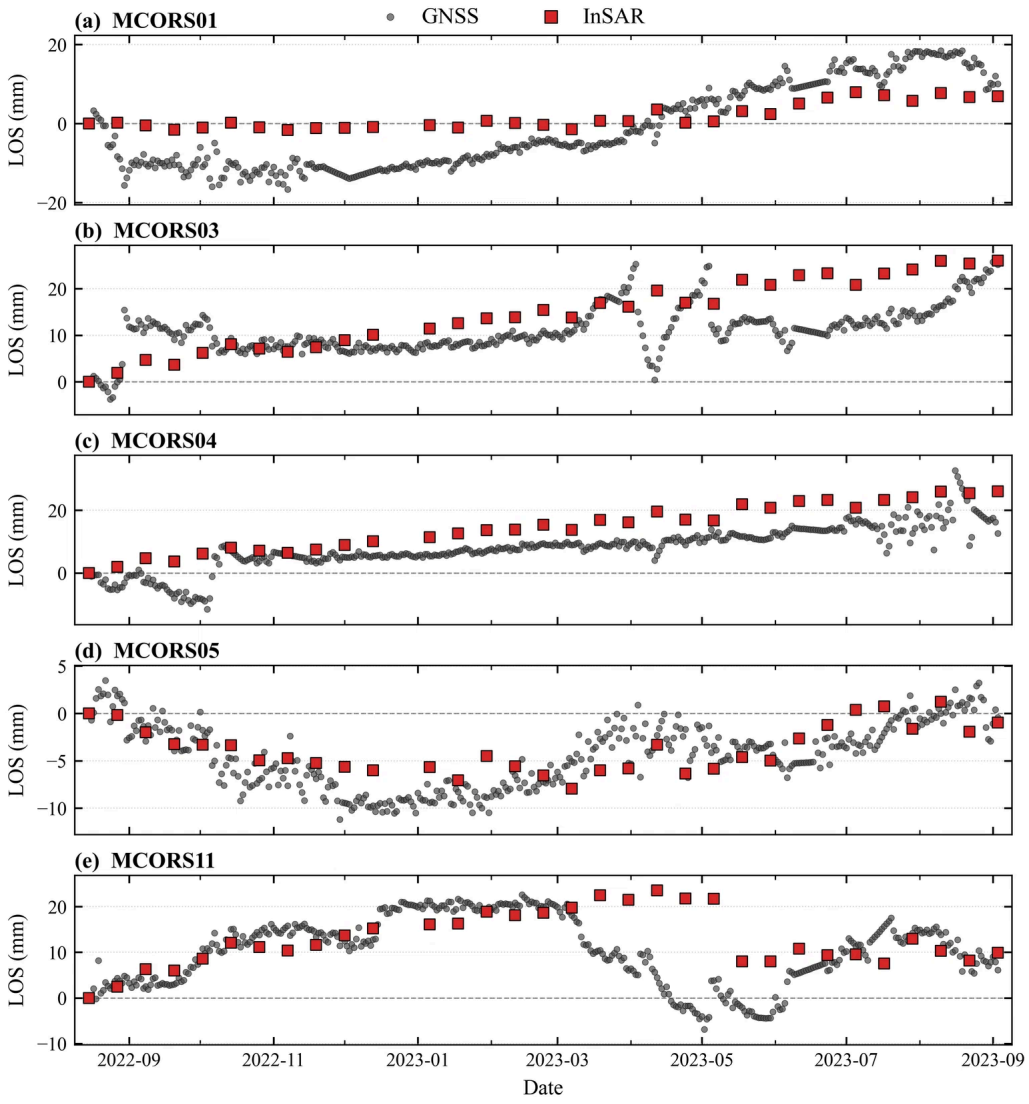


Figure 6. Comparison of LOS deformation time series between GNSS and adjacent InSAR pixels.

2.3. Fusion Method

The method presented in this paper consists of five modules: data preprocessing, basic deformation field construction, residual state estimation, deformation reconstruction, and accuracy verification, as shown in Figure 7.

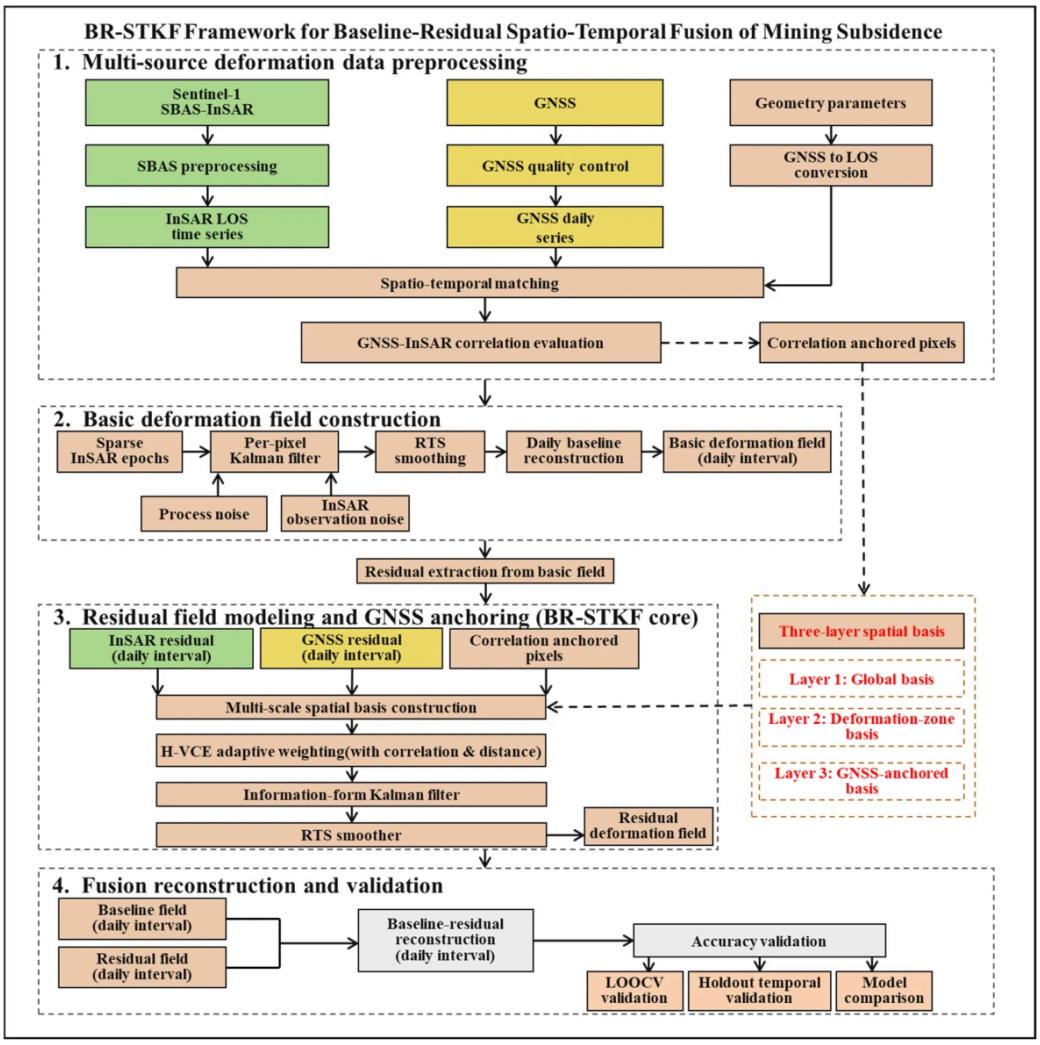


Figure 7. Overall flowchart of the BR-STKF research methodology.

This paper proposes a baseline deformation field–residual decoupled spatio-temporal KF fusion method (BR-STKF). This method achieves retrospective spatio-temporal reconstruction of LOS deformation in mining areas through the construction of a daily scale baseline deformation field, correlation-anchored multiscale bi-square spatial basis residual modeling, and relative weight adjustment via Helmert variance component estimation (H-VCE).

This paper models the InSAR-GNSS fusion process as a linear state-space system with decoupled "baseline deformation field–residual field" components. This framework comprises two core steps: (1) recovering the daily scale baseline deformation field from sparse InSAR time series using pixel-wise Kalman filtering and RTS smoothing; (2) performing state estimation of the InSAR and GNSS residual signals relative to the baseline deformation field in a low-dimensional space spanned by multiscale spatial basis functions.

Compared to directly incorporating raw InSAR and GNSS observations into a single joint filtering system, the baseline deformation field–residual decoupling strategy offers the following potential advantages; these advantages serve primarily as motivations for model design in this paper, and their numerical validity and error propagation still require further quantitative verification:

(1) Separation of information scales: The temporal sparsity of raw InSAR observations (32 phases distributed over 385 days in this study) and daily GNSS observations

may result in an imbalance in information contribution during direct joint modeling. This study first represents the main temporal information of InSAR as a daily scale baseline field, and then jointly processes the two types of observations in the residual space.

(2) Hierarchical error processing: InSAR errors (such as residual atmospheric delay, deconvolution errors, and incoherence noise) and GNSS errors (such as multipath and tropospheric residuals) exhibit different spatio-temporal statistical characteristics. The decoupling framework allows these two types of observations to be processed separately in two stages: pixel-by-pixel KF and residual KF.

(3) Signal-scale decomposition: The constant-velocity kinematic model primarily represents low-frequency, slowly varying LOS deformation components, while the spatial basis is used to describe residual structures relative to the baseline field. This decomposition reduces the apparent amplitude of the residual field; however, the baseline field and the residual field are not statistically independent. Since both components are derived from the same InSAR observation, this paper employs a two-stage serial estimation process in which the baseline field is estimated first, followed by modeling of its residuals. Therefore, the final result should be a model reconstruction based on the estimated baseline field, rather than a joint estimation of two statistically independent components. To quantitatively evaluate the coupling between the two stages, the empirical cross-correlation between the reconstructed baseline field and the residual field was calculated across all pixels, yielding an average correlation coefficient of only 0.0684. This near-orthogonal property demonstrates that error propagation from the baseline stage into the residual estimation and H-VCE weighting is negligible in practice.

2.3.1. Pixel-by-Pixel Kalman Smoothing and Construction of the Baseline Deformation Field

In the InSAR-GNSS fusion process, a common approach for extending discrete InSAR epoch observations to a daily scale grid is pixel-by-pixel linear interpolation. Mathematically, this method is equivalent to assuming that ground deformation evolves linearly at a constant rate between adjacent epochs; however, this assumption has the following limitations in practical applications:

(1) Discontinuity of the first derivative: The piecewise linear trajectories generated by linear interpolation exhibit rate jumps at epoch boundaries, whereas ground deformation typically exhibits a time-continuous and spatially smooth velocity field during normal evolution.

(2) Lack of uncertainty quantification: Linear interpolation assumes that all observation weights across time steps are equal, making it difficult to distinguish high-quality observations (high coherence, no solution entanglement errors) from low-quality observations (low coherence, containing atmospheric artifacts). When observation noise is significant, the noise may even be mapped as spurious deformation acceleration.

To address these issues, this study models the LOS deformation time series of each InSAR pixel as a dynamic system subject to kinematic constraints and performs baseline estimation under these constraints using Kalman and RTS smoothing.

The state-space model is as follows.

For each InSAR pixel, a two-dimensional state vector is defined as follows:

$$x_t^{(i)} = \begin{bmatrix} d_t^{(i)} \\ v_t^{(i)} \end{bmatrix} \in R^2 \tag{8}$$

where the two state components $d_t^{(i)}$ and $v_t^{(i)}$ represent, respectively, the cumulative displacement along the LOS (mm) and the instantaneous deformation rate (mm/day) of a given pixel on day t. $t = 0, 1, \ldots, T-1$; in this experiment, $T = 385$ days.

System equations (constant-velocity kinematic model):

$$x_t^{(i)} = \Phi x_{t-1}^{(i)} + w_t^{(i)}, w_t^{(i)} \sim N(0, Q) \tag{9}$$

The state transition matrix Φ encodes the motion constraint—today's displacement equals yesterday's displacement plus yesterday's rate multiplied by the unit time step—and the rate remains constant in the absence of external forces:

$$\Phi = \begin{bmatrix} 1 & 1 \\ 0 & 1 \end{bmatrix} \tag{10}$$

Process noise $w_t^{(i)}$ is used to characterize unmodeled changes in displacement and velocity; it follows a zero-mean Gaussian distribution $w_t^{(i)} \sim N(0, Q)$, where Q is the preset process noise covariance matrix. In this study, relatively weak process noise is set to avoid introducing excessive oscillations on days without observations.

Observation Equation:

InSAR pixels provide LOS displacement observations over 32 SAR epochs:

$$Z_{ins}(s_i, t_k) = H x_{t_k}^{(i)} + \varepsilon_{ins}^{(i)}, \varepsilon_{ins}^{(i)} \sim N\left(0, \sigma_{ins}^2\right) \tag{11}$$

$$H = \begin{bmatrix} 1 & 0 \end{bmatrix} \tag{12}$$

where $Z_{ins}(s_i, t_k)$ represents the LOS deformation observation value at the i-th InSAR pixel located in space at k-th SAR observation time; $x_{t_k}^{(i)}$ denotes the two-dimensional state vector of this InSAR pixel at the moment t_k; H is the observation matrix used to extract the one-dimensional cumulative LOS displacement component from the two-dimensional state vector; $\varepsilon_{ins}^{(i)}$ represents the observation error of i-th InSAR pixel at this SAR observation time; σ_{ins}^2 denotes the variance of the InSAR observation error; s_i indicates the spatial location of the i-th InSAR pixel; and t_k refers to the k-th SAR observation time.

That is, the InSAR directly observes the displacement component, while the velocity component is estimated through temporal filtering. This paper uniformly adopts an ob-

servational noise standard deviation of 5.00 mm as an empirical reference value. Since this setting does not explicitly account for heteroscedasticity among different pixels, coherence, and time phases, the observation weights in the baseline phase should be understood as a simplifying assumption.

The filtering process consists of two steps: prediction and update. For non-SAR epochs, only state prediction is performed; for SAR epochs, updates are made based on the prediction using InSAR LOS observations.

Subsequently, RTS backward smoothing is used to fuse information from preceding and subsequent time phases, yielding a daily scale baseline deformation field for each pixel. This processing preserves the spatial details of the InSAR data while providing continuous temporal constraints for days without SAR observations.

2.3.2. Joint Observation Model for the Basic Deformation Field and Residuals

Given a pixel-by-pixel baseline deformation field, this paper constructs both InSAR and GNSS residuals, for which the observation equations are:

$$y_I(s_i,t_k) = b(s_i,t_k) + f_I(s_i,t_k) + \varepsilon_I(s_i,t_k) \tag{13}$$

$$y_G(s_j,t) = b(s_j,t) + f_G(s_j,t) + \varepsilon_G(s_j,t) \tag{14}$$

where s_i and s_j denote the spatial positions of the i-th InSAR pixel and the j-th GNSS station, respectively; t_k(k = 1,…,32) designates the discrete acquisition dates of Sentinel-1 SAR, whereas t(t = 1,…,385) represents the continuous daily time step; $b(s,t)$ denotes the deterministic daily baseline deformation field reconstructed via pixel-wise Kalman RTS smoothing; and f_I and f_G represent the localized spatio-temporal residual deformation fields relative to the baseline.

The error terms $\varepsilon_I(s_i,t_k) \sim N\left(0,\sigma_{ins}^2\right)$ and $\varepsilon_G\left(s_j,t\right) \sim N\left(0,\sigma_{gnss}^2\right)$ are explicitly modeled as zero-mean Gaussian "effective residuals." It should be emphasized that σ_{ins}^2 and σ_{gnss}^2 do not represent pure sensor measurement noise alone. Rather, these parameters serve as effective residual variances that comprehensively absorb three distinct sources of uncertainty: (1) observational noise and environmental noise; (2) spatial point-to-pixel representativeness discrepancies; and (3) structural model mismatch and basis truncation errors inherent in the 124-dimensional spatial basis expansion. Defining these components as effective residuals establishes a mathematically rigorous and physically grounded framework for the subsequent adaptive weight estimation via H-VCE.

Regarding the two types of residuals, $f_I(s_i,t_k)$ represents the residual deformation at InSAR pixel location s_i and time t_k, obtained by subtracting the baseline deformation field b from the observed deformation y_I, while $f_G(s_j,t)$ represents the residual deformation at the j-th GNSS station location s_j and time t, obtained by subtracting the baseline deformation field b from the GNSS observations. Both are mapped to a low-dimensional state space via a shared spatial basis matrix and are uniformly described by a time-varying residual state vector. The residual state is modeled using a first-order autoregressive process to reflect the temporal persistence of the residual field.

This study employs diagonalized state transition matrices and process noise matrices. This simplified setup assumes that the baseline field already represents the primary low-frequency trends and neglects the dynamic coupling among different spatial basis coefficients to reduce the number of parameters under conditions with a limited number

of GNSS stations. This assumption does not equate to proving that the residual coefficients are mutually independent; the dependence of the results on fixed state parameters and process noise is discussed as a limitation in the "Limitations and Directions for Improvement" Section.

2.3.3. Construction of Multiscale Spatial Basis Functions Anchored by Correlation

Design Principles: Spatial basis functions are used to project the 1704-dimensional InSAR pixel residual field into a lower-dimensional space. This paper designs the spatial basis based on three aspects—multiscale completeness, local support, and GNSS adaptability—to accommodate large-scale atmospheric residuals, mesoscale settlement gradients, and local corrections around individual stations.

$$S_\delta = \begin{bmatrix} S_{L1} & S_{L2} & S_{L3} \end{bmatrix} \tag{15}$$

The Bi-square kernel function is adopted for the construction of spatial basis functions; all three layers of spatial basis functions employ the Bi-square kernel function with tight support as their basis form. For a spatial coordinate s and a basis center c_k, the function value depends on the Euclidean distance d and its influence radius R:

$$d = \| s - c_k \|_2 \tag{16}$$

$$\Phi(d;R) = \begin{cases} \left(1 - \left(\frac{d}{R}\right)^2\right)^2, & d < R \\ 0, & d \geq R \end{cases} \tag{17}$$

The Bi-square kernel function assigns spatial weights only within the influence radius R: the closer the distance, the greater the weight; when $d \geq R$, the weight is 0. This locally weighted characteristic helps describe local spatial variations and attenuates the influence of distant pixels. Although the higher-order derivatives of this function are discontinuous at the support boundaries, this does not affect the numerical orthogonalization of the spatial basis functions using QR decomposition in this paper.

The first layer consists of a 5 × 5 grid of Bi-square basis functions uniformly distributed across the entire study area, used to represent large-scale residuals and slowly varying background errors; the second layer identifies active deformation zones based on a mask of annualized LOS deformation rates ($|\text{rate}| > 10$ mm/year) and deploys a 7 × 7 grid of denser basis functions in the subsidence core and peripheral areas to better capture larger subsidence gradients; the third layer employs a GNSS correlation-based anchoring strategy, using InSAR pixels in the vicinity of each GNSS station as a candidate set. Anchor pixels are selected based on the correlation of concurrent LOS sequences, and local Bi-square basis functions are deployed at the anchored locations. This strategy reduces the impact of anomalies in a single nearest-neighbor pixel on the fusion results.

After stitching the three layers of the basis functions, a column norm screening is performed to eliminate basis functions that contribute very little to the study area's pixels. Ultimately, 124 valid basis functions are retained.

2.3.4. Helmert Variance Component Estimation and Residual State Estimation

Residual state estimation employs an information-form Kalman filter. This approach requires matrix operations only in the low-dimensional space of the basis coeffi-

cients, avoiding direct processing of the high-dimensional covariance matrix at the pixel level, which improves computational efficiency and numerical stability.

After forward filtering, this study employs fixed-rank RTS backward smoothing to further integrate full-time-series information and mitigate prediction drift during long-interval InSAR observation periods.

To reduce the subjectivity of fixed empirical weights, this paper employs Helmert variance component estimation to estimate the effective residual variances for InSAR and GNSS from the prediction residuals. This variance is used for data-driven relative weight adjustment; however, it may simultaneously include measurement noise, spatial representativeness errors, and model mismatches (e.g., a constant-velocity kinematic model struggles to describe accelerated deformation in mining activities). The correlation coefficient r is used solely for pixel selection; after screening based on a correlation threshold, the square of the correlation coefficient r is used as the spatial weight to perform a weighted average of the neighborhood InSAR residuals. The residual state estimation uses the same GNSS variance—updated via H-VCE—for all valid GNSS stations, and the residual state estimation is performed with three fixed outer-loop VCE iterations.

2.3.5. Deformation Field Reconstruction and Time-Domain Post-Processing

The fused deformation field is first obtained by adding the baseline deformation field to the estimated residual field:

$$Z_{fused}(s_i,t) = b(s_i,t) + S_\Delta(s_i) \cdot \eta_{t|T} \tag{18}$$

where $Z_{fused}(s_i,t)$ represents the fused LOS deformation at pixel s_i on day t, $b(s_i,t)$ represents the baseline deformation field, $S_\delta(s_i)$ represents the value of the spatial basis function matrix at pixel s_i, $\eta_{t|T}$ represents the smoothed residual state vector on day t via RTS smoothing, and $S_\delta(s_i) \cdot \eta_{t|T}$ represents the residual deformation component at that pixel on day t.

Subsequently, an adaptive-window Savitzky–Golay (S-G) low-pass filter is applied to the daily scale time series for each pixel:

$$w_i = max(5, min(11, T - (T \bmod 2) - 1)) \tag{19}$$

where w_i denotes the Savitzky–Golay (S-G) filter window length used for pixel s_i, T denotes the total length of the time series for that pixel, and mod denotes the modulo operation. The window length is restricted to a range of 5 to 11 and adjusted to an odd number to ensure that the filter window is centered on the current time step.

After the Kalman filter completes its daily update, some minor daily fluctuations may still remain in the time series. This paper employs a third-order S-G filter, which uses data from multiple adjacent time steps to fit a local cubic polynomial, thereby attenuating these short-term fluctuations.

3. Results

3.1. SBAS-InSAR and GNSS Preprocessing Results

To visually demonstrate the results of interferometric phase unwrapping, four interferometric pairs—numbered 11, 22, 27, and 47—were selected from a total of 68 pairs. In Figure 8, (a1) and (a2) correspond to interferogram pair 11, (b1) and (b2) correspond to interferogram pair 22, (c1) and (c2) correspond to interferogram pair 27, and (d1) and (d2) correspond to interferogram pair 47; the top row shows the wrapped phases, and the bottom row shows the corresponding unwrapped phases. After unwrapping, all four sets of examples maintained spatial continuity in the primary deformation areas, with

no large-scale isolated phase jumps observed.

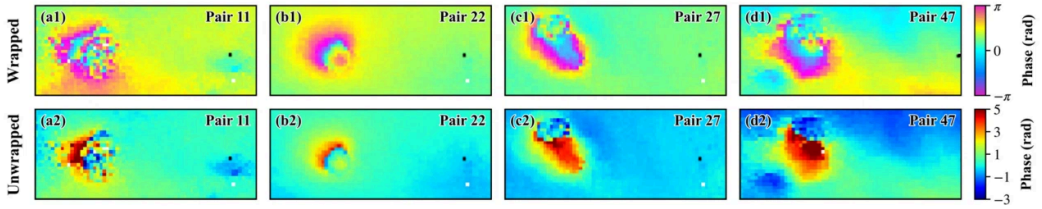


Figure 8. Comparison of the wrapped phase (**top**) and unwrapped phase (**bottom**) of a randomly selected interferogram pair.

As shown by the SBAS-InSAR processing results from Figure 9, deformation in the study area exhibits significant spatial heterogeneity, with cumulative LOS deformation ranging from −101.18 mm to +71.84 mm. Substantial changes are primarily concentrated in localized areas and are accompanied by pronounced spatial gradients, while LOS changes in the remaining areas are relatively gradual. This characteristic indicates that deformation in the study area does not follow a uniform, consistent pattern across the entire region, but rather exhibits features of localized concentration, significant spatial heterogeneity, and rapid boundary transitions. Since the SBAS-InSAR observations consist of only 32 discrete time phases, the raw results can reveal the spatial deformation patterns on each observation date but cannot directly describe the daily scale evolution between adjacent observation dates.

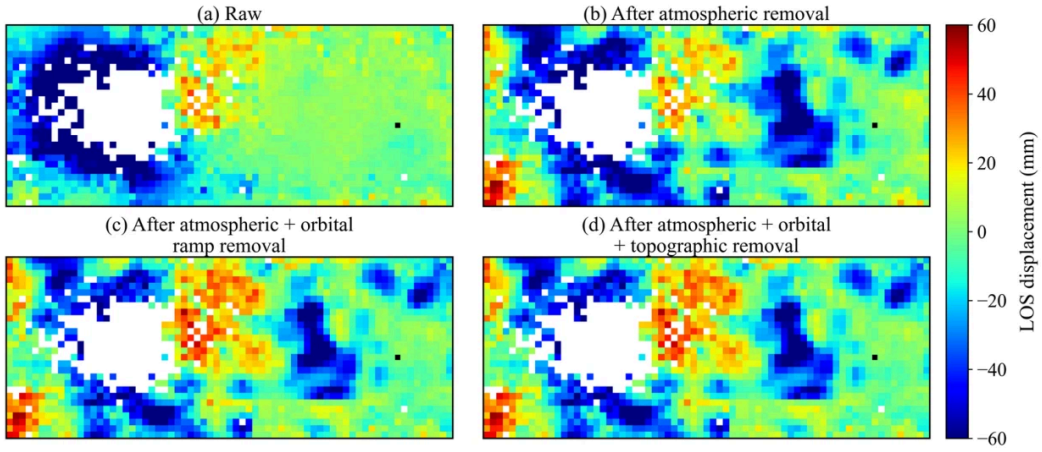


Figure 9. Cumulative-processed LOS displacements for the final phase. (**a**) Raw results; (**b**) atmospheric removal; (**c**) atmospheric and orbital ramp removal; (**d**) atmospheric, orbital, and topographic correction.

Figures 8 and 9 illustrate the data fidelity and error-mitigation procedures during InSAR preprocessing. Specifically, Figure 8 confirms the reliability of interferometric phase unwrapping across four representative pairs with distinct temporal baselines, demonstrating that spatial phase continuity is strictly maintained across the large-gradient subsidence center without phase tearing or unwrapping jumps. Figure 9 depicts the stepwise correction progression via MintPy, illustrating how raw interferometric deformation (Figure 9a)—which is severely biased by long-wavelength atmospheric phase screens and orbital ramps—is systematically rectified (Figure 9b~d) to recover the genuine, localized mining deformation field and peripheral hydrogeological responses.

Temporal coherence was used to screen valid pixels for subsequent temporal fusion. Their spatial distribution and frequency distribution is shown in Figure 10. Spatial distri-

bution of MintPy temporal coherence in the study area, the frequency distribution and hierarchical statistics of non-zero pixels are shown in Table 1. Categorized statistics of temporal coherence for non-zero valid pixels, respectively. There were a total of 1857 non-zero valid pixels in the study area, of which 1704 pixels (91.76%) satisfied $\gamma > 0.30$; pixels with $\gamma \geq 0.90$ accounted for 47.28%. Overall, high-coherence pixels dominate, while low-coherence values are primarily concentrated in localized areas.

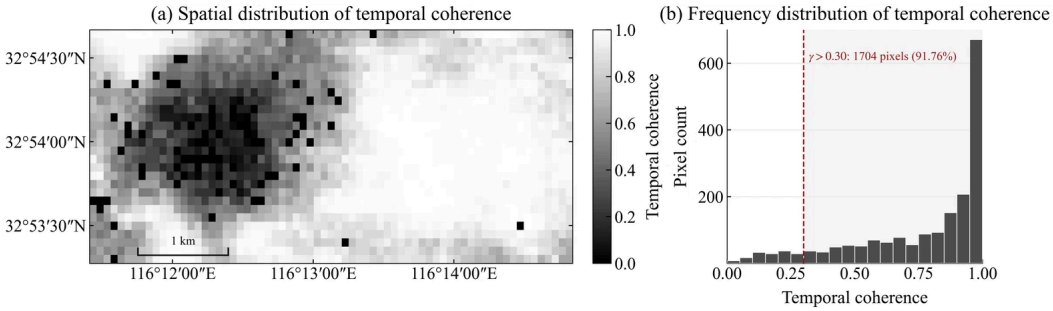


Figure 10. Temporal coherence in the study area. (**a**) Spatial distribution of temporal coherence in the study area; (**b**) frequency distribution map of temporal coherence in the study area.

Table 1. Categorized statistics of temporal coherence for non-zero valid pixels.

Quality Grade	Temporal Coherence	Number of Pixels	Percentage of Valid Pixels (%)
Lower	$0 < \gamma \leq 0.30$	153	8.24
Low	$0.30 < \gamma < 0.50$	174	9.37
Moderate	$0.50 \leq \gamma < 0.70$	263	14.16
High	$0.70 \leq \gamma < 0.80$	144	7.75
Higher	$0.80 \leq \gamma < 0.90$	245	13.19
Extremely high	$0.90 \leq \gamma \leq 1.00$	878	47.28

As shown in Table 1, pixels with $\gamma > 0.30$ account for 91.76% of the non-zero valid pixel, and high-coherence pixels dominate. Based on this overall coherence distribution, this study adopts $\gamma > 0.30$ as the pixel retention criterion to extract a 32-phase LOS cumulative deformation sequence comprising 1704 pixels, which is then spatially matched and fused with contemporaneous GNSS observations. Figure 11 shows the correlation anchoring windows for each station and the distribution of correlation coefficients for candidate pixels; Table 2 further indicates that MCORS01 and MCORS04 have higher maximum correlation coefficients, while MCORS11 has fewer usable anchoring pixels, providing local constraints of varying strengths for subsequent fusion.

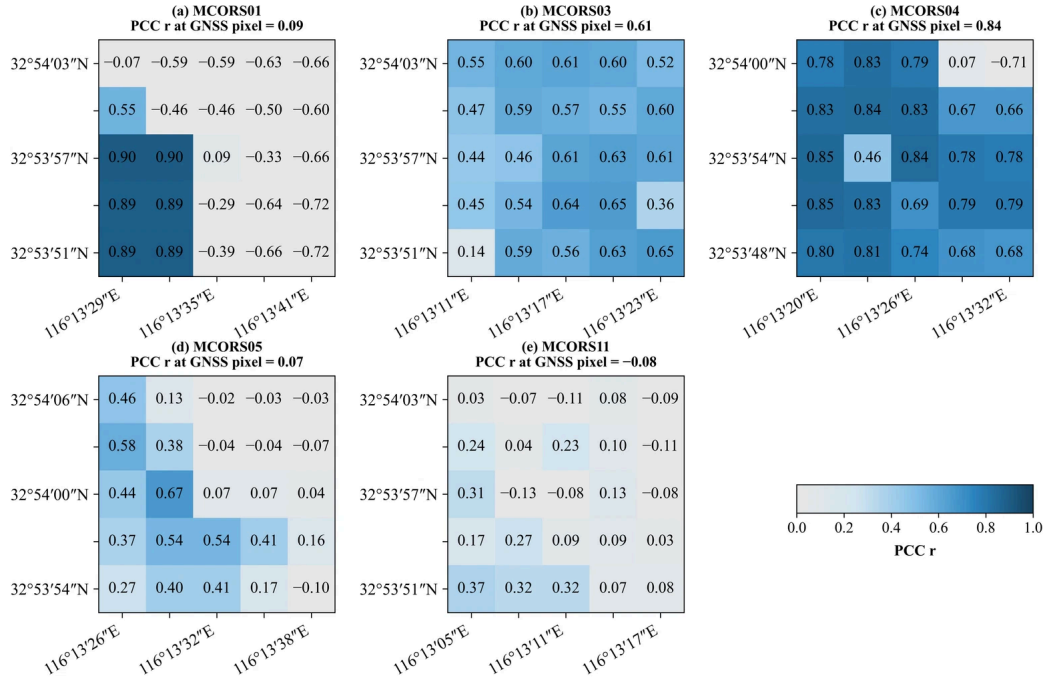


Figure 11. GNSS correlation anchoring windows and pixel correlation coefficient distributions. (**a**)~(**e**) The correlations between the deformation variables at different stations and those of their surrounding pixels.

Table 2. GNSS station correlation anchoring results.

GNSS Station	Number of Anchored Pixels	Maximum Correlation Coefficient	Average Weight
MCORS01	6	0.90	~0.17
MCORS03	19	0.65	~0.05
MCORS04	17	0.85	~0.06
MCORS05	4	0.67	~0.25
MCORS11	4	0.37	~0.25

3.2. BR-STKF Fusion Modeling and Weight Adjustment

This study utilized 32 scenes of Sentinel-1 ascending-orbit InSAR data (15 August 2022 to 3 September 2023) and daily processed LOS displacement time series from five GNSS continuous observation stations for fusion analysis. After atmospheric phase correction, removal of orbital errors, and topographic phase compensation, a 32-period cumulative LOS deformation sequence comprising 1704 highly coherent pixels was obtained, with a deformation range of −101.18 mm to +71.84 mm; the average Pearson correlation coefficient was 0.68. The temporal correlation between GNSS stations and their neighboring InSAR pixels was used to construct a GNSS correlation anchor layer, which serves as the basis for subsequent observation weight calibration.

To evaluate the reconstruction performance of BR-STKF under different spatial and temporal missing data conditions, this study selected STRE, its enhanced version eSTRE, and ISTRE, which capture large-scale spatio-temporal processes using low-rank spatial basis functions combined with temporal random effects; MOP, which utilizes multi-scale orthogonal polynomials to model multi-resolution spatial variations; STKF, which integrates state-space dynamics with Empirical Orthogonal Functions (EOF) for sequential

time-series estimation; and ST-Kriging, which extends classical geostatistics by modeling spatio-temporal variograms for spatial–temporal interpolation. These methods represent different technical approaches, including spatio-temporal random effect modeling, enhanced or robust spatial basis modeling, multiscale projection, spatio-temporal Kalman filtering based on EOF, and geostatistical interpolation. Therefore, they can be used to compare the effects of spatial basis construction, time-series state estimation, and local constraint methods on the reconstruction results.

In this paper, a total of 124 valid spatial basis functions were constructed using the BR-STKF method. The relationship between their spatial distribution and the annualized LOS deformation rate is shown in Figure 12. (a) presents uniformly distributed basis centers covering the entire domain, used to characterize regional-scale variations in residuals; (b) adds pore-scale basis functions in deformation-active zones to describe subsidence deformation gradients; (c) shows the locally anchored spatial basis filtered based on the correlation of GNSS station neighborhoods; and (d) shows the results of superimposing the three types of spatial bases, illustrating the combined relationship among the 124 basis functions in terms of global coverage, densification in active zones, and constraints near stations.

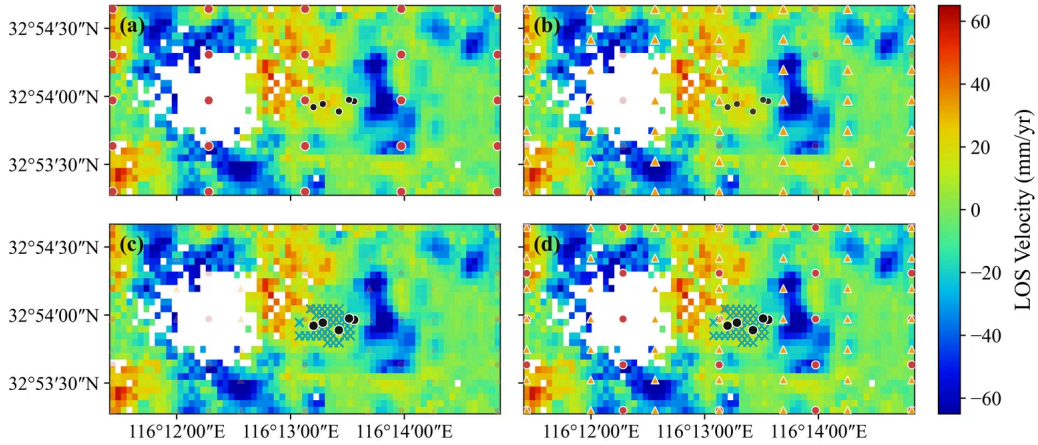


Figure 12. Spatial relationship between the BR-STKF multiscale spatial bases and annualized LOS deformation rates. (**a**) Global background centroid; (**b**) densified centroids in deformation-active areas; (**c**) GNSS correlation anchored local centroid; (**d**) result showing the superimposed three types of spatial centroids.

Table 3 shows the number of spatial basis functions used by different models. The BR-STKF uses 124 spatial basis functions, which is approximately 40% of the number used by eSTRE, and achieves a lower mean reconstruction error under the validation settings described in this paper.

Table 3. Number and types of basis functions for different models.

Model	Number of Basis Functions	Types of Basis Functions
BR-STKF	124	Three layers: global + deformation zone refinement + GNSS anchoring
STRE	74	Multiscale RBF (2 layers)
eSTRE	307	Multiscale Bi-square (Global + Local Hotspots)
ISTRE	169	Uniform Bi-square (13 × 13

Model	Number of Basis Functions	Types of Basis Functions
MOP	121	layers) Three-layer MOP (Coarse + Medium + Quad-tree-optimized Fine Layer)

In addition to the design of multiscale spatial basis functions, the H-VCE mechanism in BR-STKF can adaptively estimate the effective residual variance for both InSAR and GNSS observations. The convergence trajectories of the variance components under full-sample conditions are shown in Figure 13: the InSAR variance converges to approximately 8.00 mm^2 after the first iteration, while the GNSS variance gradually adjusts to approximately 26.65 mm^2. This variation reflects the scale of the predicted residuals under the current state model, rather than a direct separation of specific physical noise sources.

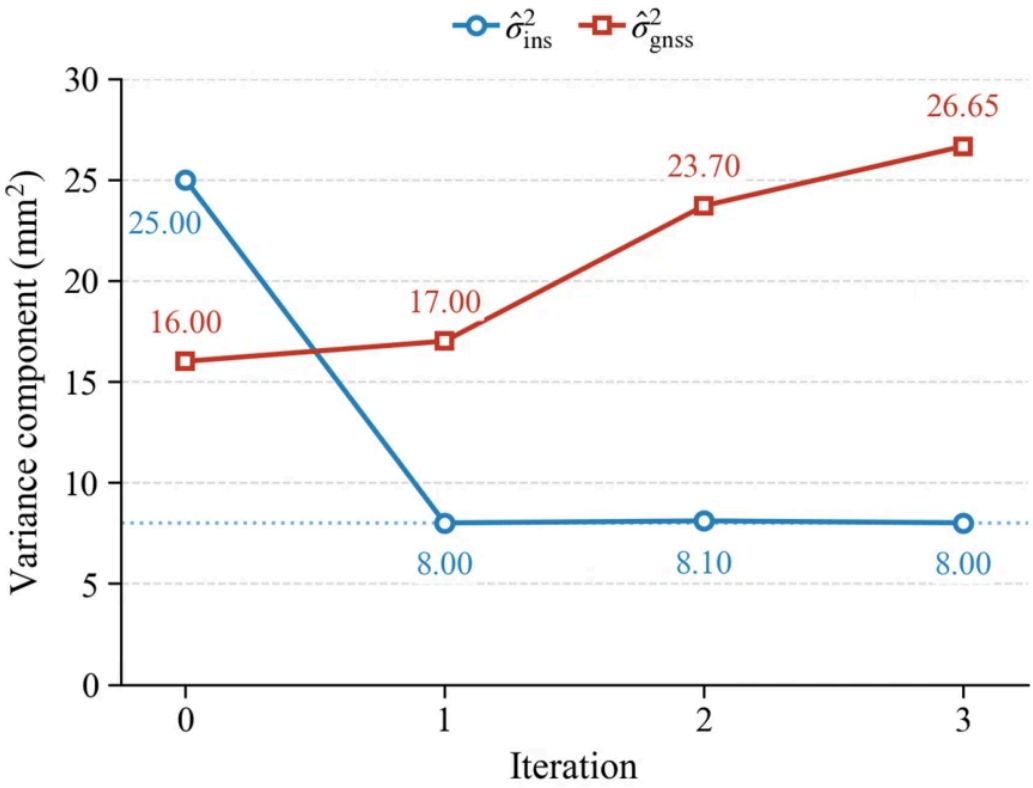


Figure 13. Convergence trajectory of H-VCE variance component estimates.

The VCE convergence process reveals two noteworthy phenomena:

(1) The variance of the InSAR effective residuals is lower than the initial empirical setting.

The InSAR effective residual variance σ^2_{ins} was adjusted from 25.00 to approximately 8.00 mm^2, indicating that, under the current baseline and residual models, the dispersion of InSAR prediction residuals is lower than the initial empirical setting.

(2) The GNSS effective residual variance is higher than the initial empirical setting.

The GNSS effective residual variance (σ^2_{gnss}) increased from 16.00 to approximately

26.65 mm^2, indicating that the predicted residuals of GNSS observations relative to the current spatial and state models are higher than the initial empirical settings.

After VCE calibration, the relative weights of InSAR and GNSS in residual fusion shifted from fixed empirical settings to estimates based on predicted residuals, thereby reducing direct dependence on the initial weights.

To evaluate the robustness of the Helmert variance component estimation (H-VCE) to initial empirical weights, sensitivity tests across several orders of magnitude were conducted. As summarized in the table above, regardless of the initial variance choices—ranging from extremely small [1.0, 1.0] to extremely large [100.0, 100.0] and asymmetric settings—the estimated variance components consistently converge to stable ranges within 3 iterations (InSAR: 7.97–8.10 mm^2, GNSS: 21.45–29.36 mm^2). This rapid and stable convergence demonstrates the exceptional robustness of the H-VCE framework, confirming that the derived relative weights are virtually independent of the initial settings, as shown in Table 4.

Table 4. Test results of the robustness and initial value sensitivity of H-VCE (units: mm^2).

Test Case	Initial InSAR	Initial GNSS	Converged InSAR	Converged GNSS
Very Small	1.0	1.0	8.04	24.67
Default	25.0	16.0	8.00	26.65
Very Large	100.0	100.0	7.98	28.14
Asymmetric-1	100.0	1.0	8.10	21.45
Asymmetric-2	1.0	100.0	7.97	29.36

Furthermore, it must be clarified that these estimated variances should be interpreted as effective residual variances rather than pure instrument measurement noise. Specifically, they comprehensively absorb multiple sources of uncertainties, including (1) observation noise; (2) spatial representativeness errors arising from point-to-pixel matching; and (3) model mismatch and truncation errors inherent in the multiscale spatial basis representation. Consequently, the resulting weights reflect the overall fitting discrepancies of the residual state model rather than isolated physical noise sources.

3.3. Evaluation of Reconstruction Results

This paper adopts a strict spatial leave-one-out cross-validation (LOOCV) scheme: in each validation fold, one GNSS station is completely held out as the unobserved target station, while only the remaining four stations participate in the model construction. Crucially, the target station is strictly isolated from all stages of the framework, including correlation anchoring, spatial basis generation, H-VCE adaptive weighting, and Kalman state updating. The spatial reconstruction capability at this unobserved site is then objectively evaluated using the RMSE between its daily reconstructed trajectory over 385 days and its actual GNSS observations.

Site Reconstruction Analysis:

Table 5 summarizes the quantitative results of the strict spatial LOOCV for the five stations, alongside a comprehensive comparison with six baseline models (STKF, eSTRE, ST-Kriging, MOP, STRE, and ISTRE). Under this rigorous spatial extrapolation protocol—where each test station is completely isolated from correlation anchoring, spatial basis construction, and weight estimation—BR-STKF achieves a competitive mean RMSE of 6.37 mm, remaining virtually on par with the spatio-temporal Kalman filter (STKF at 6.11 mm) and outperforming all other spatial basis and kriging-based models (e.g., eS-

TRE at 6.91 mm and MOP at 7.86 mm). A closer station-wise analysis reveals that BR-STKF exhibits exceptional predictive stability at specific locations, such as achieving the lowest error of 2.49 mm at MCORS05. Furthermore, BR-STKF demonstrates superior overall robustness across challenging edge or sparse locations (such as MCORS11 at 7.80 mm compared to STKF's 8.29 mm and MOP's 6.94 mm), confirming its genuine spatial generalization capability in unobserved areas without relying on local data leakage. MCORS11 is located at the edge of the study area; its GNSS-InSAR correlation coefficient is 0.32, whereas the maximum correlation coefficient for the anchor window listed in Table 2 is 0.37—these represent different statistical measures. This station exhibits relatively high errors for most models. Under the strict spatial LOOCV protocol, the RMSE of BR-STKF at this edge station is 7.80 mm, which is superior to those of STKF (8.29 mm) and eSTRE (8.73 mm), indicating that BR-STKF maintains robust reconstruction capability at complex edge locations even when local data leakage is completely eliminated.

Table 5. Reconstruction results for station-retained reconstruction using a fixed background field and training-station-anchored basis functions (LOOCV, units: mm).

Model	MCORS01	MCORS03	MCORS04	MCORS05	MCORS11	Mean
BR-STKF	7.98	6.55	7.03	2.49	7.80	6.37
STKF	8.49	5.80	5.46	2.52	8.29	6.11
eSTRE	7.65	5.88	5.43	6.86	8.73	6.91
ST-Kriging	8.35	6.41	5.79	5.48	8.60	6.93
MOP	8.59	7.49	6.40	9.86	6.94	7.86
STRE	11.53	11.71	10.44	5.12	10.67	9.89
ISTRE	16.62	8.19	8.72	15.31	11.07	11.98

ISTRE exhibits higher LOOCV RMSE values at stations such as MCORS01 and MCORS05. This phenomenon suggests that it did not achieve stable station reconstruction results under the conditions of the limited number of training stations in this study; the specific reasons still require further investigation in conjunction with weight variations and parameter sensitivity analysis.

Table 6 further provides a rigorous statistical assessment of the models, including Bootstrap 95% confidence intervals obtained through 10,000 resampling iterations, as well as paired significance tests against BR-STKF. Under the small-sample constraint, the Bootstrap 95% confidence interval of the mean RMSE for BR-STKF is [4.36, 7.72] mm, which highly overlaps with those of leading benchmarks such as STKF ([4.28, 7.87] mm) and eSTRE ([5.90, 7.98] mm). Moreover, the paired test results indicate that the numerical differences between BR-STKF and closely competing models such as STKF (p = 0.8125), eSTRE (p = 1.0000), and ST-Kriging (p = 0.6250) do not reach statistical significance ($p > 0.05$; note that for the Wilcoxon test, the theoretical minimum p-value at N = 5 is 0.0625). In contrast, BR-STKF exhibits a statistically meaningful performance improvement over conventional random-effect baselines such as STRE (paired t-test p = 0.0013). These statistical metrics confirm that, although BR-STKF lies within the top performance tier, its numerical variation relative to advanced filters should be interpreted as a descriptive performance trend rather than absolute statistical superiority, given the limited number of stations.

Furthermore, a closer examination of the station-specific results in Table 5 indicates that errors slightly increase near steep gradient or boundary zones (e.g., MCORS03 at 6.55 mm and MCORS04 at 7.03 mm), which is theoretically expected when local target-station spatial anchors are strictly isolated during basis generation. Nevertheless, com-

pared with purely data-driven baselines and standard basis models, our framework effectively suppresses error divergence through the H-VCE adaptive weighting scheme, demonstrating robust spatial generalization across previously unobserved sites.

Table 6. Quantitative performance comparison of models under strict spatial leave-one-out cross-validation.

Model	Bootstrap 95% CI	Wilcoxon *p*-Val (vs. BR-STKF)	Paired t-Test *p*-Val
BR-STKF	[4.36, 7.72]	—	—
STKF	[4.28, 7.87]	0.8125	0.5538
eSTRE	[5.90, 7.98]	1.0000	0.6309
ST-Kriging	[5.79, 8.06]	0.6250	0.4700
MOP	[6.83, 8.91]	0.6250	0.3811
STRE	[7.47, 11.43]	0.0625	0.0013
ISTRE	[8.98, 14.99]	0.0625	0.0641

The daily reconstruction time series for each station and the correspondence between the different methods and GNSS and InSAR observations are shown in Figure 14. Overall, the BR-STKF reconstruction curves effectively preserve the low-frequency trends at the five stations and provide continuous, daily scale LOS deformation estimates between discrete InSAR epochs. Compared with daily GNSS observations, the BR-STKF results are smoother, resulting in a reduced response to short-term fluctuations and local abrupt changes; compared with InSAR epoch observations, the curves generally maintain the direction of the primary cumulative changes. Compared to trend deviations or strong oscillations observed in some of the comparison methods, the BR-STKF yields relatively stable time-series reconstruction results at most stations, although the degree of adaptation varies across different stations.

Figure 14 further illustrates the temporal trajectories of surface displacement captured by different models against GNSS observations. It can be observed that conventional InSAR-only or unconstrained baseline models are susceptible to high-frequency atmospheric artifacts and temporal sampling gaps, leading to noticeable fluctuations or spurious anomalies during certain periods. In contrast, the proposed method successfully captures the nonlinear dynamic characteristics of mining subsidence—such as the transition from steady-state to accelerated settlement phases—while maintaining high trajectory smoothness. This stability is credited to the synergistic use of continuous GNSS daily observations as temporal anchors, which effectively constrain the long-term drift and bridge the sampling frequency discrepancies between radar and GNSS sensors.In the temporal dimension, this study randomly excluded 3 InSAR scenes at a time as the test phase. The remaining 29 InSAR scenes, data from all 5 GNSS stations, and observations before and after the test phase were fused, and the reconstruction RMSE for the excluded phase was calculated in the deformation-active area. To reduce the randomness of a single exclusion, the experiment was repeated three times, and the results were averaged. Since RTS smoothing and S-G filtering utilize the full time-series information, and GNSS data from the test date is still included in the fusion, this experiment evaluates retrospective conditional reconstruction with missing InSAR phases and does not represent the ability to predict the future using only past observations. The deformation-active area mask was predefined across all 32 InSAR phases and used for basis function construction; therefore, the information from the test phase was not completely isolated. This RMSE was calculated relative to the InSAR product from which the

phase was subtracted, rather than based on independent ground truth accuracy.

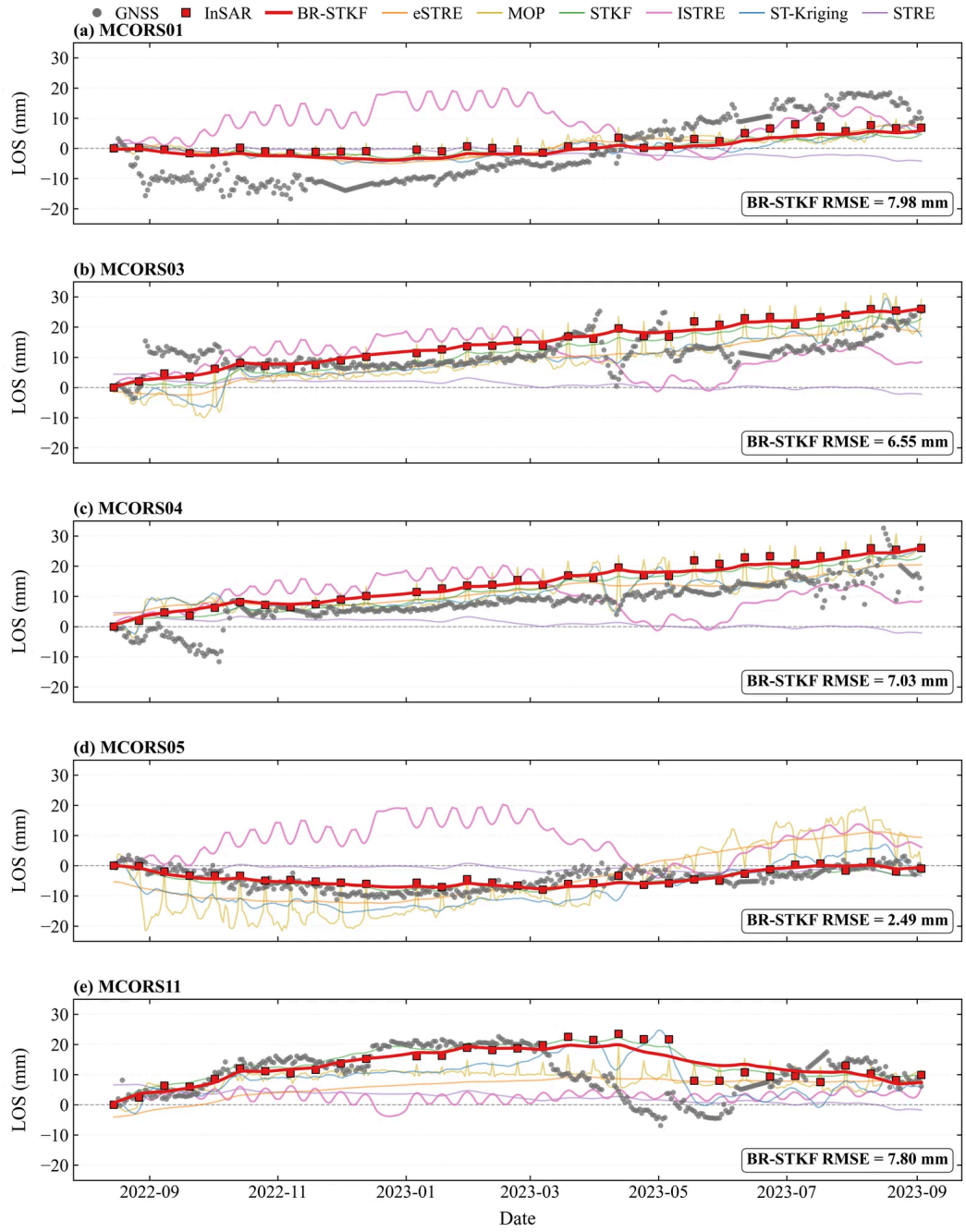


Figure 14. Temporal comparison of seven models for LOOCV station reconstruction using a fixed baseline and training station-anchored basis functions.

To further compare the retrospective reconstruction capabilities of different methods for spatial deformation fields under conditions of missing InSAR phases, Figure 15 presents spatial results for three dates: 23 February 2023; 11 June 2023; and 10 August 2023. The first row shows the InSAR spatial observation results for the corresponding dates, while the remaining rows display the reconstruction results from different methods. Across the three dates, the spatial locations of the main positive and negative LOS deformation zones in the study area remained generally consistent, but the local deformation intensity and spatial boundaries changed over time. BR-STKF was able to effectively preserve the main deformation gradients and local anomaly structures observed in

the InSAR data while continuously reconstructing missing areas. As shown in Figure 15, the RMSE values for BR-STKF on the three dates were 2.04, 3.14, and 3.65 mm, respectively—all lower than those of the other comparison methods—indicating that it achieves good spatial reconstruction performance under the experimental conditions of this study. In contrast, the reconstruction results from STRE and MOP are relatively smooth, with some local deformation features being attenuated; eSTRE, STKF, and ST-Kriging are able to preserve some local structures, but their overall errors remain higher than those of BR-STKF.

Comparing the BR-STKF results in Figure 15 with the raw InSAR observations from the same date reveals that the fused results generally preserve the locations of the main positive and negative LOS deformation zones, local high-gradient zones, and their trends over time. Compared to the original SBAS-InSAR, which provides spatial observations only at discrete phases, BR-STKF further utilizes daily GNSS observations and state models to construct a continuous daily scale deformation field between adjacent InSAR phases, enabling the conditional reconstruction of local deformation structures in the study area even when InSAR phases are missing. At the same time, the fused results are smoother than the original InSAR spatial field, and some local undulations at the pixel scale are attenuated.

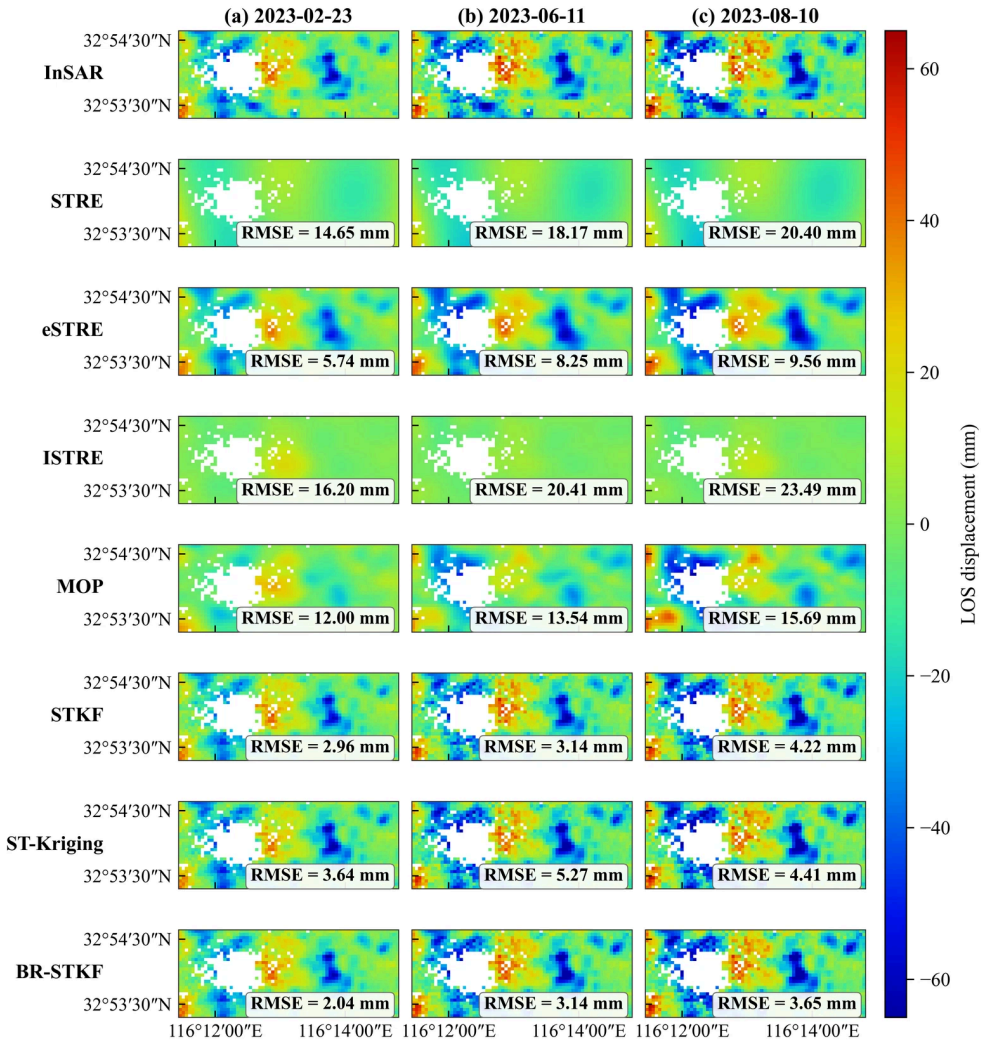


Figure 15. Spatial results from retrospective reconstruction of the Holdout phase using InSAR. (**a**)~(**c**) Reconstructions of the three dates by different models.

It is worth noting that the large discrepancies in spatial RMSE among models stem partly from differences in how each method handles unobserved boundaries and nonlinear subsidence gradients. Traditional geostatistical methods like ST-Kriging lack structural constraints for rapid, high-gradient mining deformation, leading to severe edge extrapolation errors in missing spatial phases. In contrast, BR-STKF controls local divergence through its hierarchical spatial basis and GNSS anchoring. Nevertheless, these spatial RMSE metrics are specific to the test masks of this dataset and should be interpreted as relative reconstruction performance under identical temporal test subsets rather than universal spatial accuracy bounds.

Figure 16a,b show the spatial distributions of residuals on days 192 and 384, respectively, while (c) shows the root mean square error of residuals over the 385-day period. In this paper, the residual represents the remaining deformation component of the fused deformation field relative to the baseline deformation field.

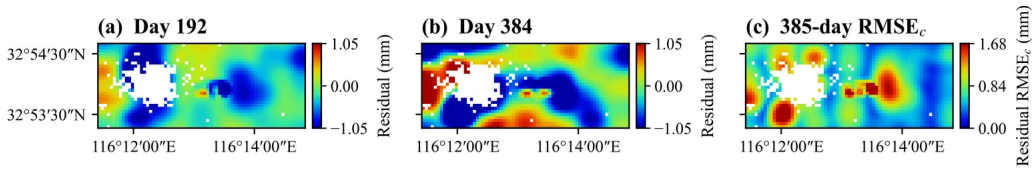


Figure 16. BR-STKF baseline deformation field–residual decomposition results. (**a**) Spatial distribution of residuals on Day 192; (**b**) spatial distribution of residuals on Day 384; (**c**) temporal $RMSE_c$ distribution of pixel residuals during the 385-day period.

The residual $RMSE_c$ in Figure 16c is calculated as follows:

$$RMSE_c = \sqrt{\frac{1}{T_i}\sum_{t \in t_i} \left(Z_{fused}\left(s_i, t\right) - b\left(s_i, t\right)\right)^2} \quad (20)$$

Here, t_i represents the set of dates on which residuals are valid for pixel s_i, and T_i is the number of valid dates, $Z_{fused}(s_i,t)$ represents the fused deformation field, and $b(s_i,t)$ represents the baseline deformation field. This $RMSE_c$ is used to describe the magnitude of residual deformation at each pixel over the study period.

The residuals at two representative times do not fully coincide in spatial location or sign; some regions show changes in residual sign across different times, indicating that residuals mainly represent time-varying local correction terms rather than fixed systematic biases. High $RMSE_c$ values are primarily concentrated in areas with large local deformation gradients or where the baseline deformation field is insufficiently represented, whereas low $RMSE_c$ values indicate that the baseline deformation field adequately explains the main temporal variations in those regions. Figure 16 illustrates how BR-STKF locally compensates the baseline deformation field using the residual field, thereby improving the fused result's ability to capture local spatial variations.

Table 7 summarizes the results of the seven methods for site-based reconstruction and retrospective reconstruction with missing InSAR phases. Under the strict spatial LOOCV, BR-STKF achieves a mean LOOCV RMSE of 6.37 mm, which remains essentially on par with models such as STKF (6.11 mm) and eSTRE (6.91 mm); meanwhile, its Holdout RMSE of 2.84 mm is substantially lower than that of the competing models in this study.

Table 7. Comparison of multi-model integration performance; LOOCV and Holdout correspond to different error metrics and spatial support scales; values are not directly ranked by accuracy within the same category.

Model	LOOCV (mm)	Holdout (mm)
BR-STKF	6.37	2.84
STKF	6.11	17.51
eSTRE	6.91	6.67
ST-Kriging	6.93	26.26
MOP	7.86	10.99
STRE	9.89	14.61
ISTRE	11.98	16.86

3.4. Ablation Study of Methodological Components

To rigorously evaluate the individual contributions of the core methodological components within BR-STKF—namely, the three-level multiscale spatial basis (MSB) representation, the GNSS correlation anchoring (CA) mechanism, and the Helmert variance component estimation (H-VCE) adaptive weighting—a progressive four-tier ablation study was conducted under identical experimental conditions:

Model 1 (Base) uses a 2-tier spatial basis representation and fixed empirical observation weights, with conventional direct station matching and without correlation anchoring.

Model 2 (+3-Tier MSB) upgrades to the 3-level multiscale spatial basis by adding local basis functions centered directly at GNSS stations, while retaining direct station matching and fixed weights.

Model 3 (+Corr-Anchor) incorporates GNSS correlation anchoring into the 3-level spatial basis and observation weighting, while retaining fixed weights.

Model 4 (Full) is the complete BR-STKF framework integrating the 3-level spatial basis, GNSS correlation anchoring, and H-VCE adaptive weighting.

As illustrated in Figure 17, the ablation results reveal distinct roles for each component:

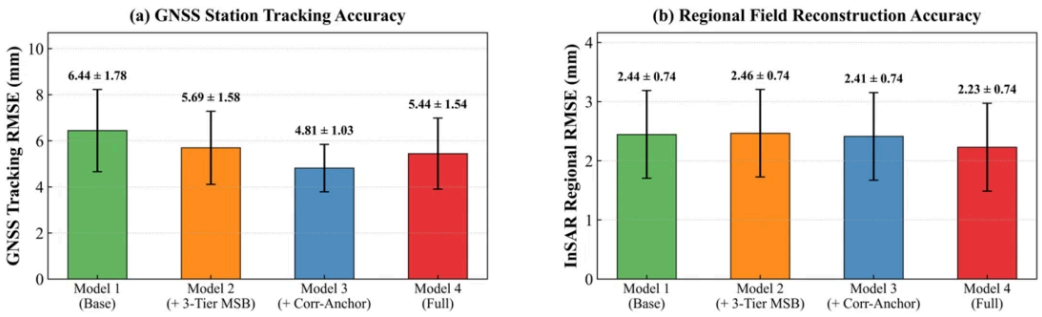


Figure 17. Ablation study results of the proposed framework variants for (**a**) GNSS tracking and (**b**) InSAR regional reconstruction.

Comparing Model 1 and Model 2, upgrading to the 3-level multiscale spatial basis via direct station-centered functions reduces the mean GNSS tracking RMSE from 6.44 mm to 5.69 mm. This confirms that adding localized spatial basis functions around stations effectively provides geometric degrees of freedom to capture local variations.

Comparing Model 2 and Model 3, the incorporation of GNSS correlation anchoring further improves local GNSS station tracking accuracy, reducing the mean GNSS tracking RMSE from 5.69 mm to 4.81 mm. This independently confirms that correlation-driven pixel filtering and weighting effectively strengthen local constraints under sparse GNSS conditions compared to naive direct station anchoring.

Comparing Model 3 and Model 4, the integration of H-VCE adaptive weighting further reduces the regional field reconstruction error, achieving a low InSAR regional RMSE of 2.23 mm. While the local GNSS tracking RMSE shows a minor adjustment, this behavior highlights a well-managed trade-off: H-VCE avoids local overfitting to individual sparse stations by objectively estimating residual variances, thereby enhancing the overall global spatial consistency and regional generalization robustness of the framework.

4. Discussion

The evaluation results demonstrate that BR-STKF achieves a competitive mean RMSE of 6.37 mm under a strict spatial LOOCV. Although its average error is numerically close to that of the spatio-temporal Kalman filter (STKF at 6.11 mm), formal statistical tests—including Bootstrap 95% confidence intervals and Wilcoxon signed-rank tests—confirm that these numerical differences do not reach statistical significance under the small sample constraint. This highlights that under sparse monitoring conditions, performance variations across leading filters reflect distinct structural trade-offs rather than absolute superiority. BR-STKF's primary advantage lies in its enhanced structural stability at complex edge locations and its robust handling of observation scale gaps. Furthermore, the sensitivity analysis of Helmert variance component estimation (H-VCE) reveals two critical insights regarding adaptive weighting: first, the variance components exhibit exceptional robustness, rapidly and reliably converging to stable ranges within 3 iterations across multiple orders of magnitude of initial values (from [1.0, 1.0] to [100.0, 100.0] and asymmetric configurations), confirming that the derived relative weights are independent of initial subjective choices. Second, these estimated parameters represent effective residual variances rather than pure instrument noise, comprehensively absorbing observation errors, point-to-pixel spatial representativeness mismatches, and truncation errors in spatial bases.

In addition, the progressive ablation study quantitatively substantiates the individual and joint necessity of the framework's core components. While the 3-tier multiscale spatial basis and correlation anchoring (Models 2 and 3) progressively strengthen local station tracking accuracy, the subsequent incorporation of H-VCE adaptive weighting (Model 4) optimizes regional field reconstruction by achieving a low InSAR regional RMSE (2.23 mm). The observed minor adjustment in local GNSS tracking during this transition exemplifies a well-managed bias-variance trade-off, where H-VCE prevents overfitting to individual sparse stations and prioritizes global spatial consistency.

The number of spatial basis functions plays a crucial role in defining the effective degrees of freedom of the model. An excessive number of basis functions, while potentially reducing fitting bias, concurrently increases estimation variance. Given the limited dataset of GNSS observations (comprising 1925 daily observation points from 5 stations over 385 days), estimating an excessive number of coefficients may result in instability in parameter solutions.

The BR-STKF captures the primary temporal evolution characteristics using a pixel-by-pixel KF and represents the residual spatial structure with 124 multiscale spatial basis functions. However, on days without SAR data, when only a limited number of GNSS observations are available to update the residual state, the estimation process remains dependent on state transitions and process noise settings. This study has not yet quantified parameter estimation variance using posterior covariance or effective degrees of freedom.

Overall, the various comparative methods demonstrate distinct error characteristics under the configuration employed in this study. The methods STRE, eSTRE, ISTRE, MOP, STKF, and ST-Kriging differ in terms of spatial basis, number of parameters, dynamic structure, and local constraint methods. These differences collectively influence the reconstruction results. The results of this study indicate that BR-STKF has a lower mean error on this dataset; however, the specific failure mechanisms of other methods cannot be determined solely based on their ranking by RMSE.

This case study supports the feasibility of BR-STKF under the current data and processing configuration. However, it is important to acknowledge the limitations related to its assumptions and scope of validation:

(1) Adaptive estimation of state transition parameters and process noise covariance. In the current residual Kalman filter framework, these parameters are predominantly determined empirically and remain constant; for instance, the state transition parameter is fixed at H = 0.99, and the process noise parameter is set at U = 0.01. Such fixed parameters may not sufficiently adapt to different regions, different deformation stages, or different levels of observation noise. Future research could incorporate the Expectation–Maximization (EM) algorithm to iteratively estimate the state transition parameters and process noise covariance based on the observation sequence and the hidden state estimates obtained from Kalman smoothing. This approach would help the model better align with the temporal variation characteristics of the actual residual field and reduce reliance on empirically set parameters.

(2) Adaptive process noise settings for individual pixels. Pixel-by-pixel KF applies a uniform process noise acceleration to all pixels (e.g., σ_a = 0.01 mm/day^2). At the center of severe subsidence, the actual deformation acceleration may be relatively large. Introducing adaptive process noise parameters linked to temporal variability helps further improve the fidelity of temporal baseline estimates.

(3) Atmospheric delay correction under complex terrain. The current uniform spatial basis functions covering the entire domain do not explicitly incorporate polynomial or atmospheric tilt correction terms. Consequently, they cannot be construed as fully addressing atmospheric tilt. Future research could incorporate DEM and physical atmospheric delay terms into the state observation operator, and verify their contributions using independent meteorological data.

(4) Improved computational efficiency. The current approach involves serial computation on a per-pixel basis, which is time-intensive. For the fusion of wide-swath, large-area Sentinel-1 deformation data, computational efficiency can be significantly improved through matrix vectorization batch processing or parallel processing using Graphics Processing Units (GPUs).

(5) Validation and Scope of Application. The spatial LOOCV is conducted under a strict spatial blind-zone extrapolation protocol, wherein the held-out GNSS station is entirely isolated from correlation anchoring, multiscale spatial basis generation, H-VCE adaptive weighting, and state updates. This ensures that the evaluation reflects genuine spatial generalization to unobserved locations without any data leakage. Nevertheless, several observational and operational constraints should be noted.

First, the spatial validation is constrained by the limited number of continuous GNSS monitoring stations available in this mining district. While BR-STKF demonstrates robust local prediction stability at these unobserved sites, evaluating its large-scale spatial transferability across more complex geological faults or multi-panel mining basins requires denser geodetic networks. Second, the temporal Holdout experiment employs bidirectional RTS backward smoothing alongside contemporaneous GNSS observations across the time series; hence, it is designed for the retrospective conditional reconstruction of historical InSAR temporal gaps rather than real-time forward forecasting. Future research will explore purely forward sequential filtering frameworks, incorporate denser multi-source observation networks, and develop analytical spatial uncertainty formulations to enhance the framework's operational deployment.

5. Conclusions

This paper proposes a baseline deformation field–residual decoupled InSAR–GNSS spatio-temporal fusion framework (BR-STKF), which decomposes the fusion task into two problems: pixel-by-pixel Kalman smoothing for baseline field construction and multiscale residual state estimation. This framework is used to jointly process LOS deformation reconstruction under conditions of temporal sparsity in InSAR and spatial sparsity in GNSS.

Under the dataset and current processing configuration used in this study, BR-STKF achieved RMSEs of 6.37 mm and 2.84 mm for stationary station reconstruction and retrospective reconstruction with missing InSAR phases, respectively. These correspond to the fitting of daily GNSS time series from five stations, the reconstruction of daily time series from remaining stations, and retrospective reconstruction within the active area relative to the masked InSAR product, respectively, with different error targets and spatial support scales. In the reported comparison configurations, BR-STKF achieved competitive reconstruction errors, though the statistical significance under small sample constraints requires broader verification.

The main contributions of this study are reflected in the following three aspects:

(1) The feasibility of the baseline deformation field–residual decoupling framework was tested in this case study. Pixel-by-pixel smoothing of the baseline field captures the primary temporal variations, while spatial basis functions describe the residual spatial structure; in retrospective reconstruction under conditions where InSAR phases are missing, BR-STKF achieved an RMSE of 2.84 mm relative to the InSAR product from which the missing data was subtracted.

(2) We introduced Helmert variance component estimation to adjust the relative weights of InSAR and GNSS based on predicted residuals, thereby reducing direct reliance on initial empirical weights.

(3) A spatial constraint mechanism based on GNSS temporal correlation is introduced. InSAR pixels in the neighborhood centered on a GNSS station are searched; pixels with consistent changes based on the temporal correlation between InSAR and GNSS are filtered, and spatial weights are constructed using this correlation, enabling the deformation reconstruction to make greater use of InSAR information consistent with GNSS observations within the station's neighborhood.

In summary, BR-STKF provides a feasible processing framework for retrospective spatio-temporal fusion of single-track InSAR and GNSS LOS observations. However, the current results are limited to the specific mining area under study; they cannot be directly interpreted as vertical or three-dimensional deformation, nor do they represent real-time future predictions. Future research will further evaluate its applicability using

more independent datasets, stricter spatial holdout validation, and varying observation conditions.

Author Contributions: Conceptualization, X.Y. (Xu Yang), Z.H., and M.Z.; methodology, X.Y. (Xu Yang), Z.H., and J.Y.; software, X.Y. (Xu Yang), Z.H. and X.Y. (Xuexiang Yu); validation, X.Y. (Xu Yang), Z.H., M.Z. and X.Y. (Xuexiang Yu); formal analysis, X.Y. (Xu Yang), Z.H., and J.Y.; investigation, X.Y. (Xu Yang), Z.H., L.W., Y.G. and S.N.; resources, X.Y. (Xu Yang), Z.H., M.Z. and X.Y. (Xuexiang Yu); data curation, X.Y. (Xu Yang), Z.H. and M.Z.; writing—original draft preparation, X.Y. (Xu Yang) and Z.H.; writing—review and editing, X.Y. (Xu Yang), Z.H., J.Y., M.Z., X.Y. (Xuexiang Yu), L.W., Y.G. and S.N.; visualization, J.Y., Z.H., X.Y. (Xu Yang), and Y.G.; supervision, Y.G. and S.N.; project administration, X.Y. (Xu Yang), X.Y. (Xuexiang Yu) and L.W.; funding acquisition, X.Y. (Xu Yang) and L.W. All authors have read and agreed to the published version of the manuscript.

Funding: This work was supported by the Key Laboratory of Aviation-aerospace-ground Cooperative Monitoring and Early Warning of Coal Mining-induced Disasters of Anhui Higher Education Institutes (Anhui University of Science and Technology) (Grant No. KLAHEI202204), the National Natural Science Foundation of China (Grants No. 42304050 and 52474194), and the Engineering Research Center of Mining Area Environmental and Disaster Cooperative Monitoring (Anhui University of Science and Technology) (Grant No. KSXTJC202403).

Data Availability Statement: The data that support the findings of this study are not publicly available due to legal restrictions. The authors do not have the legal right or permission to distribute these data.

Acknowledgments: The authors acknowledge the European Space Agency and the Copernicus program for providing the Sentinel-1 data and the Copernicus DEM GLO-30 product; we also thank the Anhui Banji Coal Mine for providing the GNSS monitoring data.

Conflicts of Interest: The authors declare no conflicts of interest.

References

1. Cai, Y.; Jin, Y.; Wang, Z.; Chen, T.; Wang, Y.; Kong, W.; Xiao, W.; Li, X.; Lian, X.; Hu, H. A Review of Monitoring, Calculation, and Simulation Methods for Ground Subsidence Induced by Coal Mining. *Int. J. Coal Sci. Technol.* **2023**, *10*, 32. [Google Scholar] [CrossRef]
2. Unlu, T.; Akcin, H.; Yilmaz, O. An Integrated Approach for the Prediction of Subsidence for Coal Mining Basins. *Eng. Geol.* **2013**, *166*, 186–203. [Google Scholar] [CrossRef]
3. Yang, Z.F.; Li, Z.W.; Zhu, J.J.; Hu, J.; Wang, Y.J.; Chen, G.L. ANALYSING THE LAW OF DYNAMIC SUBSIDENCE IN MINING AREA BY FUSING INSAR AND LEVELING MEASUREMENTS. *Int. Arch. Photogramm. Remote Sens. Spat. Inf. Sci.* **2013**, *XL-7/W1*, 163–166. [Google Scholar] [CrossRef]
4. Lian, X.; Shi, L.; Kong, W.; Han, Y.; Fan, H. Residual Subsidence Time Series Model in Mountain Area Caused by Underground Mining Based on GNSS Online Monitoring. *Int. J. Coal Sci. Technol.* **2024**, *11*, 27. [Google Scholar] [CrossRef]
5. Kharisova, O.; Kharisov, T. Searching for Possible Precursors of Mining-Induced Ground Collapse Using Long-Term Geodetic Monitoring Data. *Eng. Geol.* **2021**, *289*, 106173. [Google Scholar] [CrossRef]
6. Tondaś, D.; Kazmierski, K.; Kapłon, J. Real-Time and Near Real-Time Displacement Monitoring With GNSS Observations in the Mining Activity Areas. *IEEE J. Sel. Top. Appl. Earth Obs. Remote Sens.* **2023**, *16*, 5963–5972. [Google Scholar] [CrossRef]
7. Bo, H.; Li, Y.; Tan, X.; Dong, Z.; Zheng, G.; Wang, Q.; Yu, K. Estimation of Ground Subsidence Deformation Induced by Underground Coal Mining with GNSS-IR. *Remote Sens.* **2022**, *15*, 96. [Google Scholar] [CrossRef]
8. Chen, Y.; Yu, S.; Tao, Q.; Liu, G.; Wang, L.; Wang, F. Accuracy Verification and Correction of D-InSAR and SBAS-InSAR in Monitoring Mining Surface Subsidence. *Remote Sens.* **2021**, *13*, 4365. [Google Scholar] [CrossRef]
9. Guo, J.; Zhang, G.; Song, Y.; Bai, Y.; Wang, J.; Wu, W.; Ge, Z. Times Series InSAR Deformation Monitoring of Jinchuan Mining Area Based on Mini Stack Technology. *Sci. Rep.* **2026**, *16*, 5327. [Google Scholar] [CrossRef] [PubMed]

10. Wassie, Y.; Milillo, P. Interferometric Synthetic Aperture Radar Multitemporal Deformation Monitoring: A Review of Machine Learning Techniques. *IEEE Geosci. Remote Sens. Mag.* **2025**, *13*, 220–243. [Google Scholar] [CrossRef]
11. Bai, Z.; Zhao, F.; Wang, J.; Li, J.; Wang, Y.; Li, Y.; Lin, Y.; Shen, W. Revealing Long-Term Displacement and Evolution of Open-Pit Coal Mines Using SBAS-InSAR and DS-InSAR. *Remote Sens.* **2025**, *17*, 1821. [Google Scholar] [CrossRef]
12. Wang, T.; Wang, Y.; Zhao, F.; Du, S.; Zhang, N.; Zhang, K.; Shen, Z.; Fernández, J. A Fusion Framework of 3D Physical Model and InSAR Monitoring for Mining-Induced Deformation Analysis. *Int. J. Appl. Earth Obs. Geoinf.* **2026**, *146*, 105122. [Google Scholar] [CrossRef]
13. Massonnet, D.; Feigl, K.L. Radar interferometry and its application to changes in the Earth's surface. *Rev. Geophys.* **1998**, *36*, 441–500. [Google Scholar] [CrossRef]
14. Ferretti, A.; Prati, C.; Rocca, F. Permanent Scatterers in SAR Interferometry. *IEEE Trans. Geosci. Remote Sens.* **2001**, *39*, 8–20. [Google Scholar] [CrossRef]
15. Lanari, R.; Mora, O.; Manunta, M.; Mallorqui, J.J.; Berardino, P.; Sansosti, E. A Small-Baseline Approach for Investigating Deformations on Full-Resolution Differential SAR Interferograms. *IEEE Trans. Geosci. Remote Sens.* **2004**, *42*, 1377–1386. [Google Scholar] [CrossRef]
16. Crosetto, M.; Monserrat, O.; Cuevas-González, M.; Devanthéry, N.; Crippa, B. Persistent Scatterer Interferometry: A Review. *ISPRS J. Photogramm. Remote Sens.* **2016**, *115*, 78–89. [Google Scholar] [CrossRef]
17. Kinoshita, Y. Development of InSAR Neutral Atmospheric Delay Correction Model by Use of GNSS ZTD and Its Horizontal Gradient. *IEEE Trans. Geosci. Remote Sens.* **2022**, *60*, 5231414. [Google Scholar] [CrossRef]
18. Wang, Y.; Yunjun, Z.; Wang, N.; Liu, R.; Liang, C.; Aoki, Y.; Wang, R. Towards Long-Wavelength Ionospheric Correction of InSAR Time Series Using GNSS-Based TEC. *IEEE Trans. Geosci. Remote Sens.* **2026**, *64*, 5202314. [Google Scholar] [CrossRef]
19. Yan, H.; Lu, Z.; Li, Y.; Wang, R.; Li, F.; Tang, Q. InSAR Atmospheric Error Correction Method Based on GNSS Spatial Interpolation With Application to the Southern North Island of New Zealand. *IEEE Trans. Geosci. Remote Sens.* **2026**, *64*, 4100815. [Google Scholar] [CrossRef]
20. Bekaert, D.P.S.; Segall, P.; Wright, T.J.; Hooper, A.J. A Network Inversion Filter combining GNSS and InSAR for tectonic slip modeling. *J. Geophys. Res. Solid Earth* **2016**, *121*, 2069–2086. [Google Scholar] [CrossRef]
21. Farolfi, G.; Bianchini, S.; Casagli, N. Integration of GNSS and satellite InSAR data: Derivation of fine-scale vertical surface motion maps of the Po Plain, Northern Apennines, and Southern Alps, Italy. *IEEE Trans. Geosci. Remote Sens.* **2019**, *57*, 319–328. [Google Scholar] [CrossRef]
22. Wu, X.; Shao, Y.; Yang, Z.; Lan, L.; Bian, X.; Liu, M. Integration of InSAR and GNSS Data: Improved Precision and Spatial Resolution of 3D Deformation. *Remote Sens.* **2026**, *18*, 142. [Google Scholar] [CrossRef]
23. Dai, S.; Zhang, Z.; Li, Z.; Liu, X.; Chen, Q. Prediction of Mining-Induced 3-D Deformation by Integrating Single-Orbit SBAS-InSAR, GNSS, and Log-Logistic Model (LL-SIG). *IEEE Trans. Geosci. Remote Sens.* **2023**, *61*, 5222213. [Google Scholar] [CrossRef]
24. Tao, Q.; Liu, R.; Li, X.; Gao, T.; Chen, Y.; Xiao, Y.; He, H.; Wei, Y. A Method for Monitoring Three Dimensional Surface Deformation in Mining Areas Combining SBAS-InSAR, GNSS and Probability Integral Method. *Sci. Rep.* **2025**, *15*, 2853. [Google Scholar] [CrossRef] [PubMed]
25. Ma, F.; Yu, K.; Zhang, J.; Zhang, J.; Lian, W.; Zhang, Q.; Zhao, Z.; Zhang, H. Study on Three-Dimensional Deformation Inversion in Mining Areas Based on PIM Optimized by CMA-ES and Multi-Source InSAR. *Remote Sens.* **2026**, *18*, 1839. [Google Scholar] [CrossRef]
26. Yang, Z.; Li, Z.; Zhu, J.; Yi, H.; Hu, J.; Feng, G. Deriving Dynamic Subsidence of Coal Mining Areas Using InSAR and Logistic Model. *Remote Sens.* **2017**, *9*, 125. [Google Scholar] [CrossRef]
27. Hu, J.; Yan, Y.; Dai, H.; He, X.; Lv, B.; Han, M.; Zhu, Y.; Zhang, Y. Prediction Method for Dynamic Subsidence Basin in Mining Area Based on SBAS-InSAR and Time Function. *Remote Sens.* **2024**, *16*, 1938. [Google Scholar] [CrossRef]
28. Liu, N.; Dai, W.; Santerre, R.; Hu, J.; Shi, Q.; Yang, C. High Spatio-Temporal Resolution Deformation Time Series With the Fusion of InSAR and GNSS Data Using Spatio-Temporal Random Effect Model. *IEEE Trans. Geosci. Remote Sens.* **2019**, *57*, 364–380. [Google Scholar] [CrossRef]
29. Shi, Q.; Dai, W.; Santerre, R.; Li, Z.; Liu, N. Spatially Heterogeneous Land Surface Deformation Data Fusion Method Based on an Enhanced Spatio-Temporal Random Effect Model. *Remote Sens.* **2019**, *11*, 1084. [Google Scholar] [CrossRef]
30. Yan, H.; Dai, W.; Xie, L.; Xu, W. Fusion of GNSS and InSAR Time Series Using the Improved STRE Model: Applications to the San Francisco Bay Area and Southern California. *J. Geod.* **2022**, *96*, 47. [Google Scholar] [CrossRef]

31. Li, P.; Li, Z.; Mao, W.; Shi, Q.; Lin, Q. Fusion of InSAR and GNSS Based on Adaptive Spatio-Temporal Kalman Model for Reconstructing High Spatio-Temporal Resolution Deformation. *IEEE J. Sel. Top. Appl. Earth Obs. Remote Sens.* **2024**, *17*, 19616–19626. [Google Scholar] [CrossRef]
32. Yan, H.; Dai, W.; Liu, H.; Gao, H.; Neely, W.R.; Xu, W. Fusion of Spatially Heterogeneous GNSS and InSAR Deformation Data Using a Multiresolution Segmentation Algorithm and Its Application in the Inversion of Slip Distribution. *Remote Sens.* **2022**, *14*, 3293. [Google Scholar] [CrossRef]
33. Tondaś, D.; Ilieva, M.; Van Leijen, F.; Van Der Marel, H.; Rohm, W. Kalman Filter-Based Integration of GNSS and InSAR Observations for Local Nonlinear Strong Deformations. *J. Geod.* **2023**, *97*, 109. [Google Scholar] [CrossRef]
34. Teunissen, P.J.G.; Amiri-Simkooei, A.R. Least-Squares Variance Component Estimation. *J. Geod.* **2008**, *82*, 65–82. [Google Scholar] [CrossRef]
35. Cressie, N.; Johannesson, G. Fixed Rank Kriging for Very Large Spatial Data Sets. *J. R. Stat. Soc. Ser. B Stat. Methodol.* **2008**, *70*, 209–226. [Google Scholar] [CrossRef]
36. Cressie, N.; Shi, T.; Kang, E.L. Fixed-rank filtering for spatio-temporal data. *J. Comput. Graph. Stat.* **2010**, *19*, 724–745. [Google Scholar] [CrossRef]
37. Li, Z.; Ding, X.; Pu, Z.; Yan, X.; Pang, L.; Liu, K.-X. Technology for Proactive Regional Control of Roof Water Hazards in Ultra-Thick, Loose Aquifers. *Coal Eng.* **2025**, *57*, 80–87. [Google Scholar]
38. Berardino, P.; Fornaro, G.; Lanari, R.; Sansosti, E. A New Algorithm for Surface Deformation Monitoring Based on Small Baseline Differential SAR Interferograms. *IEEE Trans. Geosci. Remote Sens.* **2002**, *40*, 2375–2383. [Google Scholar] [CrossRef]
39. Li, D.; Deng, K.; Gao, X.; Niu, H. Monitoring and Analysis of Surface Subsidence in Mining Areas Based on SBAS-InSAR. *Geomat. Inf. Sci. Wuhan Univ.* **2018**, *43*, 1531–1537. [Google Scholar] [CrossRef]
40. Zheng, Y.; Zhao, Z.; Zeng, M.; Zhou, D.; Su, X.; Liu, D. Monitoring and Analysis of Surface Deformation in the Buzhaoba Open-Pit Mine Based on SBAS-InSAR Technology. *Remote Sens.* **2024**, *16*, 4177. [Google Scholar] [CrossRef]
41. Yunjun, Z.; Fattahi, H.; Amelung, F. Small Baseline InSAR Time Series Analysis: Unwrapping Error Correction and Noise Reduction. *Comput. Geosci.* **2019**, *133*, 104331. [Google Scholar] [CrossRef]
42. Fialko, Y.; Simons, M.; Agnew, D. The complete 3-D surface displacement field in the epicentral area of the 1999 Mw 7.1 Hector Mine earthquake, California, from space geodetic observations. *Geophys. Res. Lett.* **2001**, *28*, 3063–3066. [Google Scholar] [CrossRef]

Disclaimer/Publisher's Note: The statements, opinions and data contained in all publications are solely those of the individual author(s) and contributor(s) and not of MDPI and/or the editor(s). MDPI and/or the editor(s) disclaim responsibility for any injury to people or property resulting from any ideas, methods, instructions or products referred to in the content.